Atmospheric
Chemistry
and Physics
Discussions

Radiative forcing by volcanic eruptions since 1990, calculated with a chemistry-climate model and a new emission inventory based on vertically resolved satellite measurements

Jennifer Schallock[1], Christoph Brühl[1], Christine Bingen[2], Michael Höpfner[3], Landon Rieger[4], and Jos Lelieveld[1]

[1]Atmospheric Chemistry Department, Max Planck Institute for Chemistry, Mainz, Germany
[2]Royal Belgian Institute for Space Aeronomy, Brussels, Belgium
[3]Institute of Meteorology and Climate Research, Karlsruhe Institute of Technology, Karlsruhe, Germany
[4]Institute of Space and Atmospheric Studies, University of Saskatchewan, Saskatoon, Canada

Correspondence: Jennifer Schallock (jennifer.schallock@mpic.de)

Abstract.

This paper presents model simulations of stratospheric aerosols with a focus on explosive volcanic eruptions. Using various (occulation and limb based) satellite instruments, with vertical profiles of sulfur dioxide (SO_2) from the MIPAS (Michelson Interferometer for Passive Atmospheric Sounding) instrument and vertical profiles of aerosol extinction from GOMOS (Global Ozone Monitoring by Occultation of Stars), OSIRIS (Optical Spectrograph and InfraRed Imaging System), and SAGE II (Stratospheric Aerosol and Gas Experiment), we characterised the influence of volcanic aerosols for the period between 1990 and 2019.

We established a volcanic sulfur emission inventory that includes more than 500 eruptions. The identified SO_2 perturbations were incorporated as three-dimensional pollution plumes into a chemistry-climate model, which converts the gases into aerosol particles and computes their optical properties. The Aerosol Optical Depth (AOD) and the climate radiative forcing are calculated online. Combined with model improvements, the simulations reproduce the observations of the various satellites.

Slight deviations between the observations and model simulations were found only for the large volcanic eruption of Pinatubo in 1991. This is likely due to either an overestimation of the removal of aerosol particles in the model, or limitations of the satellite measurements, which are related to saturation effects associated with anomalously high aerosol concentrations. Since Pinatubo, only smaller-sized volcanic eruptions have taken place. Weak- and medium-strength volcanic eruptions captured in satellite data and the Smithsonian database typically inject about $10\,kt$ to $50\,kt$ SO_2 directly into the upper troposphere/lower stratosphere (UTLS) region or transport it indirectly via convection and advection. Our results show that these relatively smaller eruptions, which occur quite frequently, can nevertheless contribute significantly to the stratospheric aerosol layer and are relevant for the Earth's radiation budget. These eruptions are found to cause a global radiative forcing in the order of $-0.1\,Wm^{-2}$ at the tropopause.

Atmospheric
Chemistry
and Physics
Discussions

Open Access

EGU

1 Introduction

Excluding recent history in which large fires have become a major source of aerosols up to the tropopause and above it, stratospheric aerosol particles are mostly of volcanic origin and consist of a mixture of liquid sulfuric acid (H_2SO_4) and water (H_2O) droplets, which are condensed from the gas phase by secondary particle formation. The typical median diameter of these

25   aerosol particles ranges between 200 nm for the background aerosol and 600 nm for Pinatubo conditions (Brühl et al., 2015). As species with a relatively long lifetime, stratospheric aerosol particles show a tendency to accumulate in the lower stratospheric aerosol layer at altitudes of between 15 km and 25 km (Junge et al., 1961). At these heights, they scatter the incoming solar radiation in the ultraviolet (UV), visible and near-infrared (IR) ranges and absorb the outgoing terrestrial mid-infrared radiation, in this way influencing the radiation budget of the Earth's atmosphere. In this study, we incorporated stratospheric aerosol,

30   including the sulfur budget, the sulfur chemistry and the radiative transfer into a comprehensive Chemistry Climate Model (CCM), which we have used to gain a better understanding of the interaction of aerosols with the global climate system and ozone. Much focus is currently being placed on adequately modelling and understanding the impact of volcanic eruptions and other aerosol sources on the evolution of the stratospheric aerosol burden.

Sulfate and ashes from explosive volcanic eruptions can account for the majority of the aerosol burden in the stratosphere

35   during volcanically active periods and cause strong temporal and spatial variations in the concentration and the size distribution of the particles. These changes influence in turn the radiative forcing at tropopause altitudes (or at the top of the atmosphere) and can even have a large impact on the global climate for one to three years after the eruptions (Timmreck, 2012). Due to the large variability in volcanic emissions, it is not possible to define future trends for stratospheric optical depth and forcing. Therefore, the influence of volcanic eruptions is not included in predictive simulations for future climate scenarios in the

40   IPCC report from 2013 (IPCC, 2013). Previous studies show that model simulations often cannot completely reproduce the AOD of satellite observations or the global forcing of the stratospheric aerosol layer (Solomon et al., 2011), because the number of volcanic eruptions reaching the stratosphere is underestimated in most analyses (Mills et al., 2016; Brühl et al., 2015). Conversely, the intensity of single eruptions is sometimes overestimated because of incorrect vertical distribution of the injection patterns in the models. Smaller volcanic eruptions have often been underestimated in previous studies (Brühl

45   et al., 2015), even though they can be responsible for radiative forcing that is twice as strong as the background conditions in volcanically quiescent periods such as from 1999 to 2002 (IPCC, 2013). Therefore, sulfur dioxide (SO_2) injections into the stratosphere from previously underestimated and unknown volcanic eruptions have to be recalculated based on the most recent releases of satellite data sets, in particularly those gathered using limb sounding instruments to derive information in the vertical direction.

50   Non-eruptive permanently degassing volcanoes represent a smaller natural source of aerosols, which are treated separately from active explosive volcanic eruptions. Stratospheric H_2SO_4 is also produced from non-volcanic sulfur precursor gases, like carbonyl sulfide (OCS) (Crutzen, 1976), dimethyl sulfide (DMS) (Kettle and Andreae, 2000), and tropospheric SO_2 from pollution, constituting a background concentration of stratospheric aerosol. To improve the accuracy of the sulfur budget of the stratosphere in the CCM, sources and sinks of sulfur as well as its precursor gas components have to be identified.

Atmospheric
Chemistry
and Physics
Discussions

55   The relevant processes of the stratospheric aerosol life cycle are structured in this paper as follows: section 2 presents satellite data used for entering the volcanic perturbations of aerosols and SO_2 into the model, and for model evaluation. In section 3, the setup used for the climate model simulations is described. Section 4 contains a volcanic sulfur emission inventory with all relevant explosive volcanic eruptions detected between 1990 and 2019, which are included in the model simulations in section 5. The influence of these volcanic eruptions on the stratosphere and climate is analysed in section 6. At the end of

60   section 6 as well as in the final discussion (section 7), the results are discussed in a wider context.

2   Satellite observations

We analysed satellite data sets from two instruments on the European Environmental Satellite (ENVISAT) that was launched on 1 March 2002 and lost signal on 8 April 2012, namely MIPAS and GOMOS. Furthermore, the OSIRIS instrument on board the Odin satellite was used to provide additional data for the period up to 2019. For the period before 2002, we used the SAGE II

65   instrument. Additional SO_2 column data from the Ozone Monitoring Instrument (OMI), Total Ozone Mapping Spectrometer (TOMS), Ozone Mapping and Profiler Suite (OMPS) and other satellites were also used to verify the consistency of the data and to fill in data gaps, marked as white areas in all satellite images.

2.1   Michelson Interferometer for Passive Atmospheric Sounding (MIPAS)

MIPAS was a mid-infrared emission spectrometer on board the ENVISAT satellite. MIPAS scanned the limb, thereby analysing

70   the infrared radiation emitted by the Earth's atmosphere at different tangent altitudes (Fischer et al., 2008).

The atmospheric spectra ranging from $4.15\,\mu$m to $14.6\,\mu$m are inverted to provide vertical profiles of temperature and volume mixing ratios of more than 25 different trace species, like the sulfate aerosol precursor gases SO_2 and OCS (Glatthor et al., 2015, 2017; Höpfner et al., 2013, 2015), as well as H_2O, ozone (O_3), methane (CH_4), nitrous oxide (N_2O), nitrogen dioxide (NO_2) and nitric acid (HNO_3), among others.

75   Vertical SO_2 profiles (Figure 1) from the MIPAS SO_2 single profile retrieval (Höpfner et al., 2015) were used to identify plumes of volcanic eruptions. We utilised a gridded dataset from these retrievals with a three-dimensional sampling of $60°$ longitude, $10°$ latitude, $1\,$km altitude with a vertical coverage of $10\,$km to $23\,$km and a temporal averaging of five days. The lower altitude limit varies with the tops of clouds in the troposphere, especially in tropical regions.

The typical estimated random uncertainty for a single measurement of a volume mixing ratio profile is estimated to be

80   70–$100\,$ppt$_v$. For the gridded dataset used here, systematic uncertainties are more important. These were estimated to be 10–$75\,$ppt$_v$ (10–$180\,\%$) under background concentrations and 10–$110\,$ppt$_v$ (10–$75\,\%$) under volcanic influence (Höpfner et al., 2015). Directly after strong volcanic eruptions, the detected mass of SO_2 may be underestimated due to saturation of the limb observations as well as the applied cloud clearing scheme (Höpfner et al., 2015).
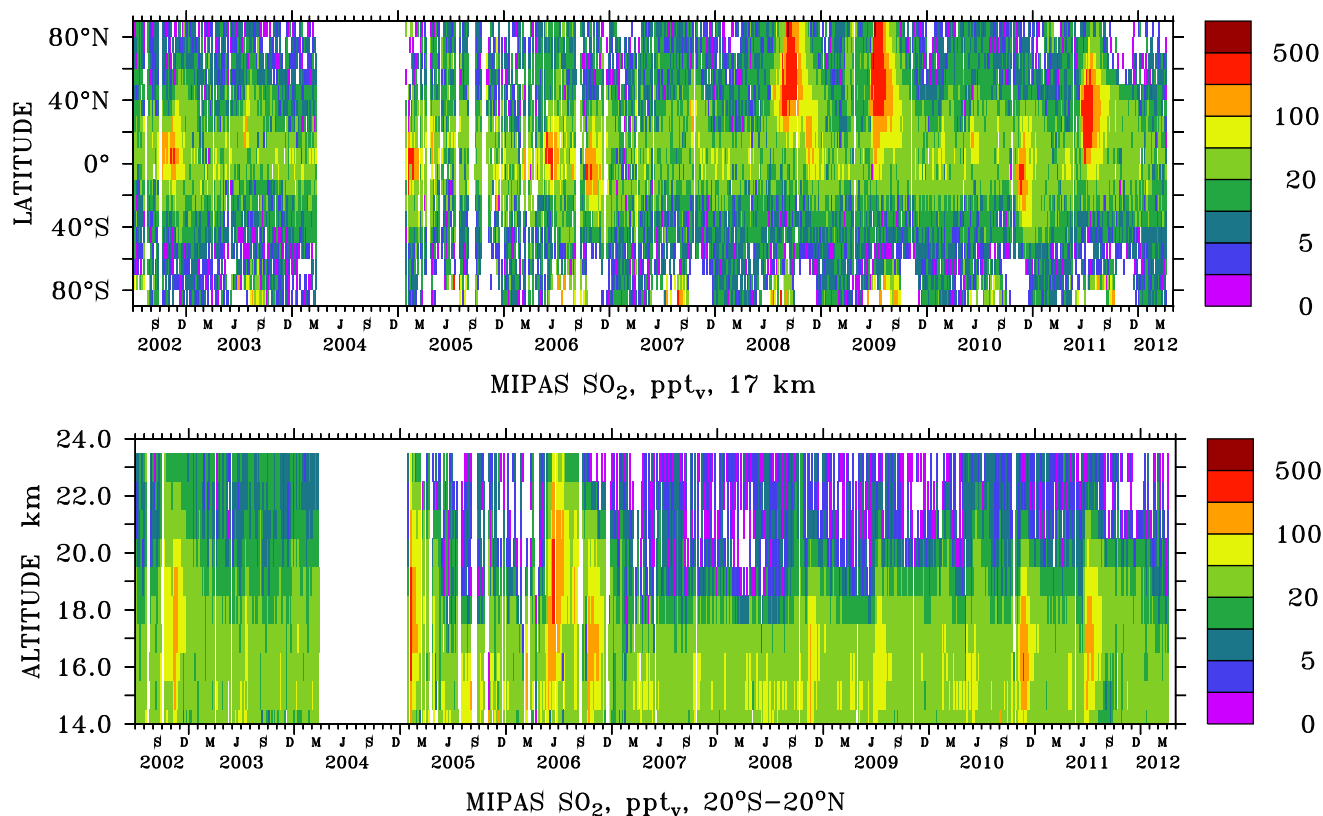
Figure 1. The volume mixing ratios of SO_2 in ppt_v (parts per trillion by volume (10^{-12})) as derived from the MIPAS instrument (Höpfner et al., 2015). The dataset spans the period 1 July 2002–8 April 2012: Horizontal distribution at 17 km altitude (top) and vertical distribution for tropical regions 20° S–20° N (bottom). White: no data.

2.2 Global Ozone Monitoring by Occultation of Stars (GOMOS)

85 The Global Ozone Monitoring by Occultation of Stars (GOMOS) instrument on ENVISAT operates based on the principle of stellar occultation. GOMOS provides data on stratospheric aerosol extinction as well as O_3, NO_2, nitrogen trioxide (NO_3) and air density. The instrument also retrieves the H_2O and oxygen (O_2) target species in the near-infrared region (Kyrölä et al., 2010). The principle of stellar occultation is described in detail in Bertaux et al. (2010). In short, this self-calibrating sounding method scans the atmosphere by pointing to a star during its sunset or sunrise. The measured spectra vary with the tangent

90 altitude due to the absorption and scattering of light by the different atmospheric species along the line of sight. In a first step, the GOMOS inversion algorithm determines the slant column density of gaseous species and the slant aerosol optical depth along the optical path (Vanhellemont et al., 2004). This process makes use of reference absorption spectra of the main absorbing species (such as the ones provided by the MPI-Mainz UV/VIS Spectral Atlas of Gaseous Molecules of Atmospheric Interest (http://satellite.mpic.de/spectral_atlas) and extinction cross-section values representative for aerosols. In a second step,

95 vertical density profiles of the target gas species and vertical profiles of the aerosol extinction coefficient are obtained from the
slant quantities (Bertaux et al., 2010).

GOMOS uses four spectrometers providing measurements at wavelengths from the UV-visible to the near-IR range in four spectral regions: 248 nm–371 nm, 387 nm–693 nm, 750 nm–776 nm, and 915 nm–956 nm (Robert et al., 2016). As the original inversion algorithm (the operational algorithm IPF) was poorly effective for the retrieval of the aerosol extinction

100 coefficient and only one extinction channel was obtained at the reference wavelength of 550 nm (Vanhellemont et al., 2010), a new retrieval algorithm called AerGOM was designed (Vanhellemont et al., 2016; Robert et al., 2016) in order to improve the spectral inversion. Also, the cross-section spectra were revised using up-to-date reference spectra (Bingen et al., 2019). AerGOM provides the spectral dependence of the aerosol extinction coefficient between about 350 nm and 750 nm.
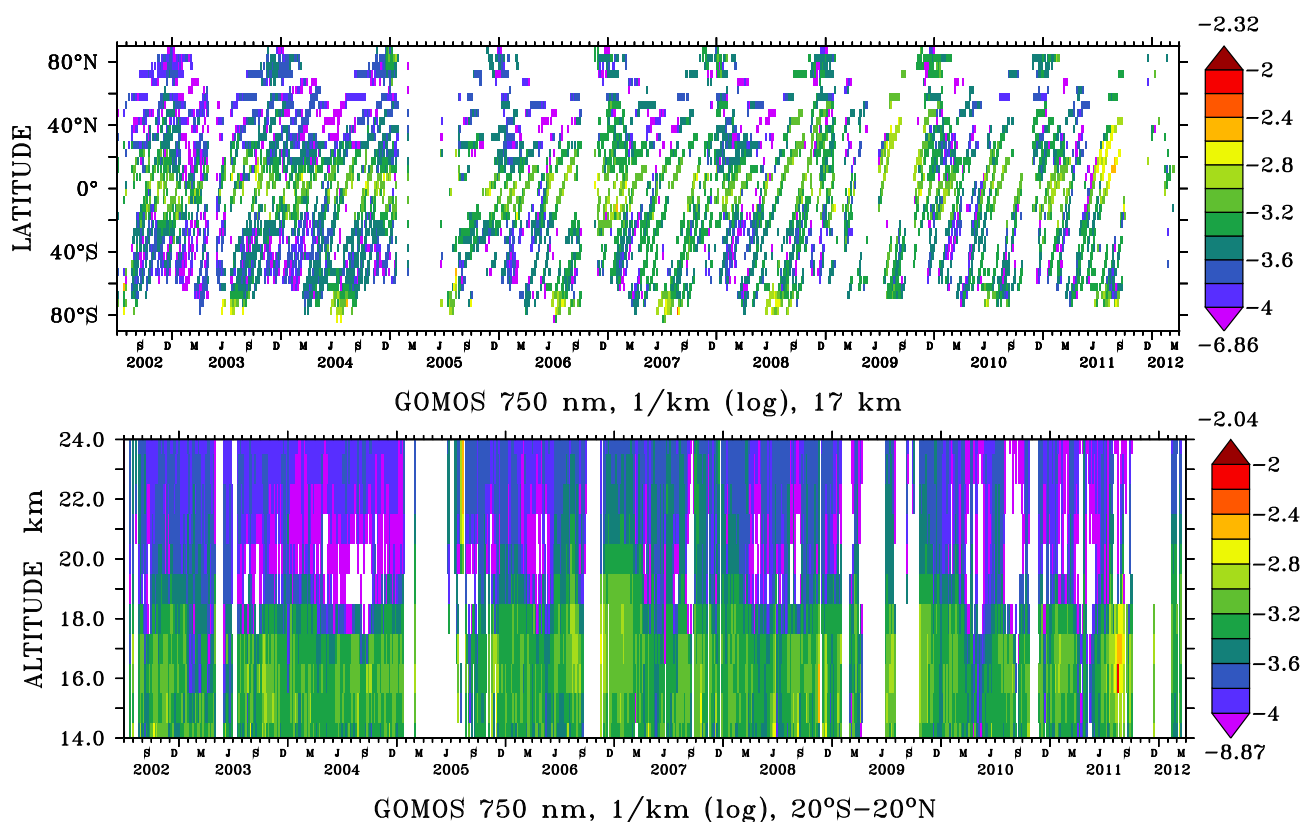

GOMOS 550 nm, 1/km (log), 17 km

GOMOS 550 nm, 1/km (log), 20°S–20°N
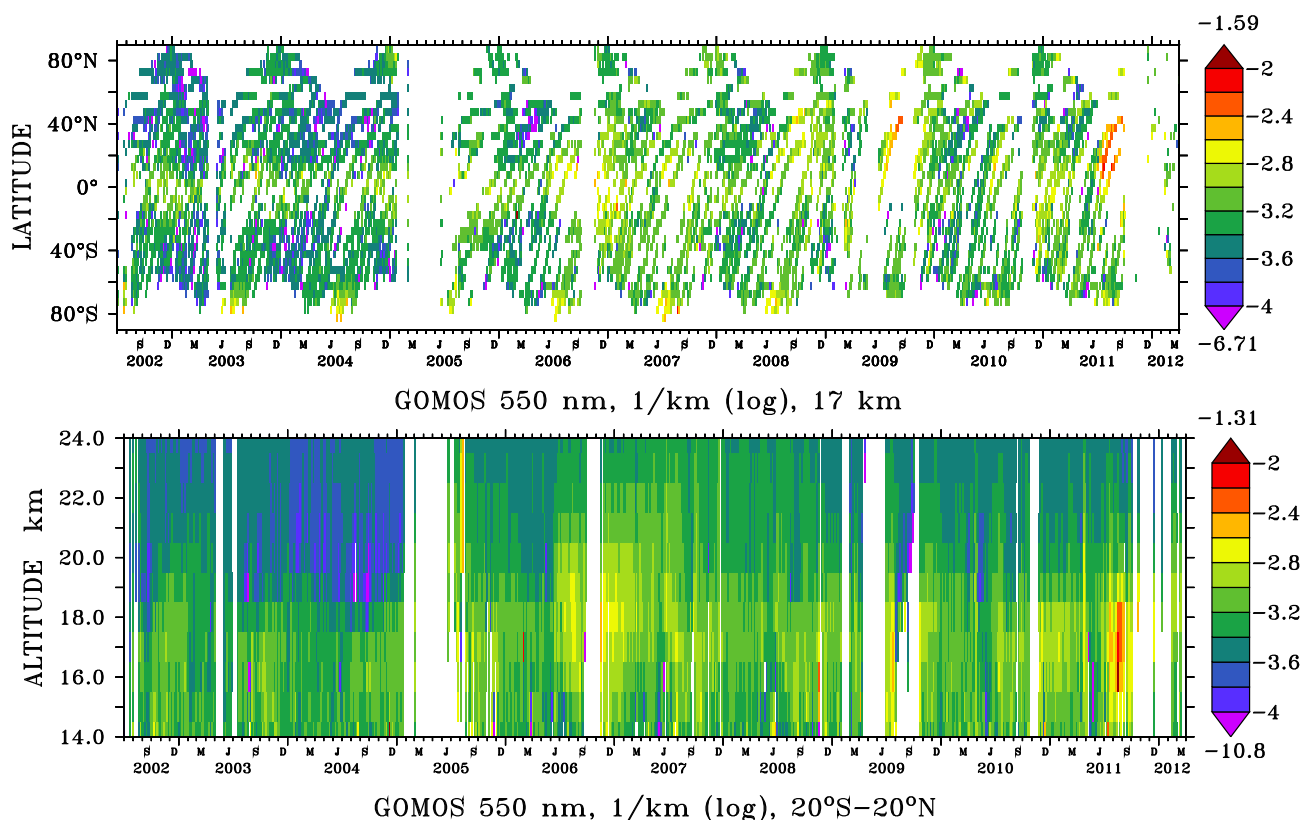
Figure 2. The decadal logarithm (log) of the aerosol extinction coefficient (1/km) as derived from the GOMOS instrument data v.3.00 at **550 nm wavelength** from Bingen et al. (2017). The dataset spans the period 15 April 2002–8 April 2012: Horizontal distribution at 17 km altitude (top) and vertical distribution for tropical regions 20° S–20° N (bottom). Maximum and minimum values appear above (dark red) and below (violet) the colour keys, respectively. White: no data.

The typical extinction uncertainty exhibits large variability in the function of the star parameters (from about 5–15 % in the

105 most favourable cases of bright, hot stars, to about 40–70 % in the less favourable cases of dim, cold stars) (Bingen et al.,

Atmospheric
Chemistry
and Physics
Discussions

2017). A full validation of AerGOM, version 1.0, is presented by Vanhellemont et al. (2016). A main factor influencing the uncertainty is the weakness of the star signal, which is alleviated by the high measurement rate made possible by the abundance of stars. The large variability in magnitude and temperature of the occulted stars also significantly influences the measurement uncertainty (Robert et al., 2016).

110   From AerGOM, climate data records were processed for use in chemistry-climate models (Bingen et al., 2017), and these are the data sets used in the present study. Figure 3 illustrates these Level-3 gridded GOMOS aerosol extinction records in version 3.00 of the algorithm, described in Bingen et al. (2017) and shows the aerosol extinction from the GOMOS instrument at wavelengths of 550 nm (Figure 2) and 750 nm.

Figure 3. The decadal logarithm (log) of the aerosol extinction coefficient (1/km) as derived from the GOMOS instrument data v.3.00 at **750 nm wavelength** from Bingen et al. (2017). The dataset spans the period 15 April 2002–8 April 2012: Horizontal distribution at 17 km altitude (top) and vertical distribution for tropical regions 20° S–20° N (bottom). Maximum and minimum values appear above (dark red) and below (violet) the colour keys, respectively. White: no data.

The grid resolution was optimized to a grid of 5° latitude by 60° longitude and a time resolution of five days. This choice

115   is made possible by the high measurement rate and is more suitable for describing the aerosol distribution than zonal monthly means, because it allows detection of the signature of aerosol patterns with a lifetime of as short as a week (e.g., medium-sized

volcanic eruptions). The GOMOS dataset is very important for compensating for data missing from the MIPAS instrument (subsection 2.1), where several important eruptions in 2004 and 2006 could not be identified (Bingen et al., 2017).

The SO_2 mixing ratio perturbation is derived from the extinction perturbation observed in a 10-day period beginning about

120   a week after the eruption by dividing by air density, multiplying by a constant and subtracting a typical background.

2.3 Optical Spectrograph and InfraRed Imaging System (OSIRIS)

The dataset from the Optical Spectrograph and InfraRed Imaging System (OSIRIS) allowed us to extend the time series beyond April 2012, after which the signal of the ENVISAT satellite was lost. OSIRIS is a limb scatter instrument, which was launched on board the Odin satellite on 20 February 2001 and is still operating today.

Figure 4. The logarithm log(1/km) of the aerosol extinction as derived from the OSIRIS instrument at **750 nm wavelength** by Bourassa et al. (2012) and Rieger et al. (2019). The dataset spans the period 1 July 2002–31 December 2019: Horizontal distribution at 17 km altitude (top) and vertical distribution for tropical regions 20° S–20° N (bottom). Maximum and minimum values appear above (dark red) and below (violet) the colour keys, respectively. White: no data.
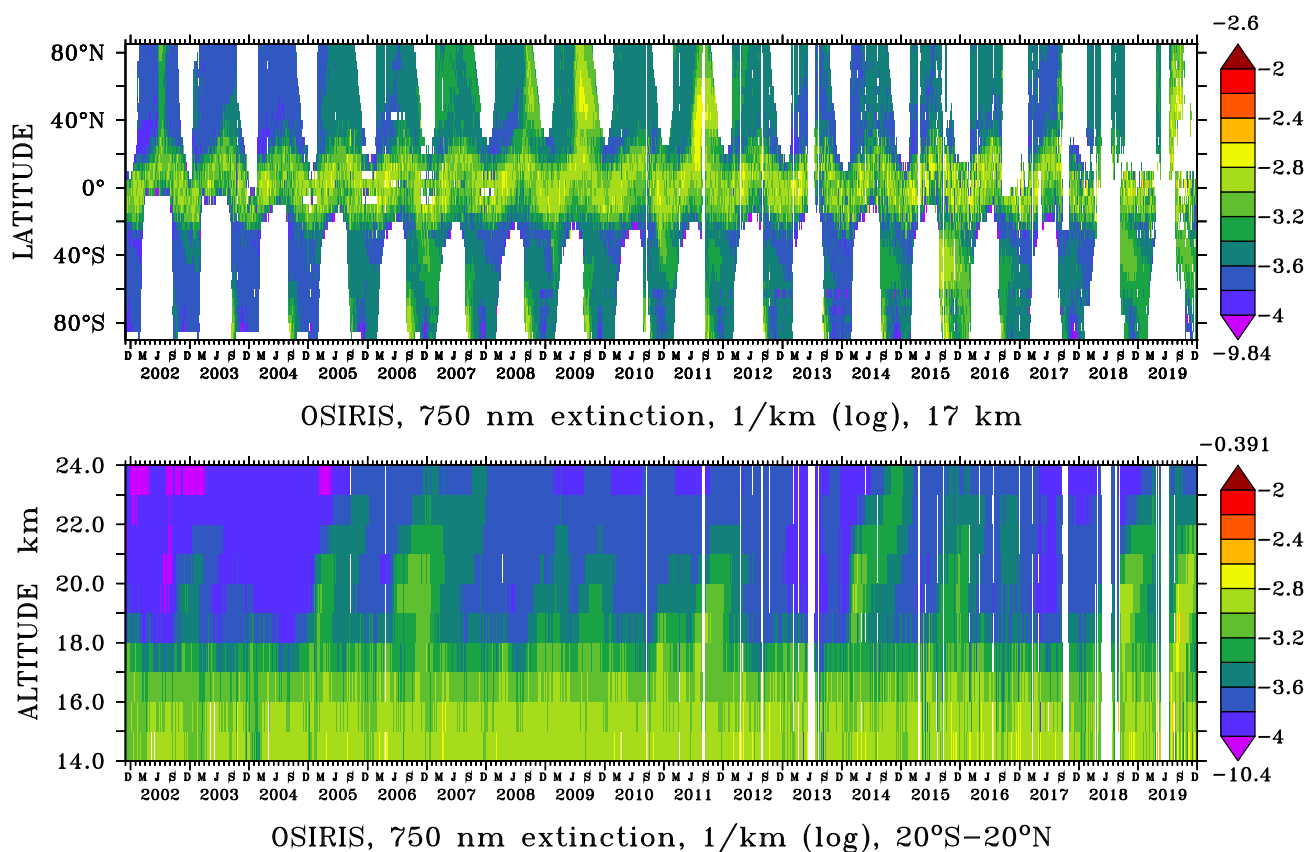
125   OSIRIS performs limb scans of atmospheric radiance spectra at wavelengths from the UV to the near-IR ranges (274 nm–810 nm) (Bourassa et al., 2012). To obtain the vertical profiles of aerosol extinction at altitudes from 10 km to 35 km (Rieger et al., 2015), the aerosol scattering properties are calculated with a refractive index of $1.427 + i7.167 \times 10^{-8}$ using Mie theory at 750 nm wavelength and a sulfate concentration of 75 % H_2SO_4 and 25 % H_2O (Rieger et al., 2018).

For this study, the OSIRIS version 5.10 aerosol retrieval was used until October 2017 and the version 7.1a afterwards (for
130   details see Rieger et al. (2019); Bourassa et al. (2012)). OSIRIS provides a surface coverage from 82° S–82° N, except in polar winter when there is no sunlight (see Figure 4). The vertical grid resolution is 1 km altitude, 5° latitude and 30° longitude with 5-day-averaged time intervals.

The total uncertainty is about 10–15 % in the aerosol layer between 15–30 km, where the sensitivity of the measurements decreases with increasing optical depth. Due to measurement noise, the uncertainty dominates the signal above 30 km and in
135   the troposphere (Rieger et al., 2015). At lower altitudes near the tropopause, the OSIRIS instrument is more sensitive to cloud perturbation than MIPAS and GOMOS, as can be seen in Figure 4 (bottom), and the uncertainty is higher.

The SO_2 mixing ratio perturbation is derived from the extinction perturbation observed over a 10-day period beginning about a week after the eruption by dividing by air density, multiplying by a constant and subtracting a typical background. If data gaps cause a shift of the time period away from the maximum perturbation or a bias in the zonal average, a correction factor is
140   applied, which can be as high as 5 if the shift is three months as for Calbuco. Correction factors up to 2 have to be applied in some cases because of cloud perturbation or incomplete profiles.

2.4   Stratospheric Aerosol and Gas Experiment II (SAGE II)

SAGE II was a solar occultation instrument that performed measurements during sunrise and sunset. The SAGE II aerosol extinction measurements on board the Earth Radiation Budget Satellite (ERBS) started in October 1984 and ended in August
145   2005. This data set is important for the model setup before the ENVISAT period starting in 2002. The aerosol extinction gridded using 60° longitude and 10° latitude intervals is derived from the V7.00 L2 profiles provided by the Earth Observing System Data and Information System of NASA (EOSDIS) database (Figure 5).

The gridded SAGE II dataset used in the present study provides a near-global coverage with latitudes between 80° N to 80° S, with a horizontal grid resolution of 60° in longitude, 10° in latitude and a vertical resolution of 0.5 km between 13 km
150   and 30 km altitude. SAGE II measured in occultation, thus, its measuring principle is similar to that of GOMOS. The two main differences between GOMOS and SAGE II, are that the latter used the sun as light source, which results in a much better signal-to-noise ratio. On the other hand, its measurement rate is much lower than that of GOMOS, since only two measurements (one sunrise and one sunset) are possible per orbit, so that a near-global coverage is achieved in about one month.

Measurements occur at seven wavelengths between 386 nm and 1020 nm. The vertical profiles of O_3, NO_2 and water vapor
155   are provided as well as aerosol extinction coefficients at four wavelengths (386, 452, 525 and 1020 nm) from the middle troposphere to the upper stratosphere. An estimate of the aerosol surface area density (SAD) is derived from the extinction coefficients (Thomason et al., 2008). From the SAD, the SO_2 mixing ratio is derived using the parameterisation of Grainger et al. (1995).
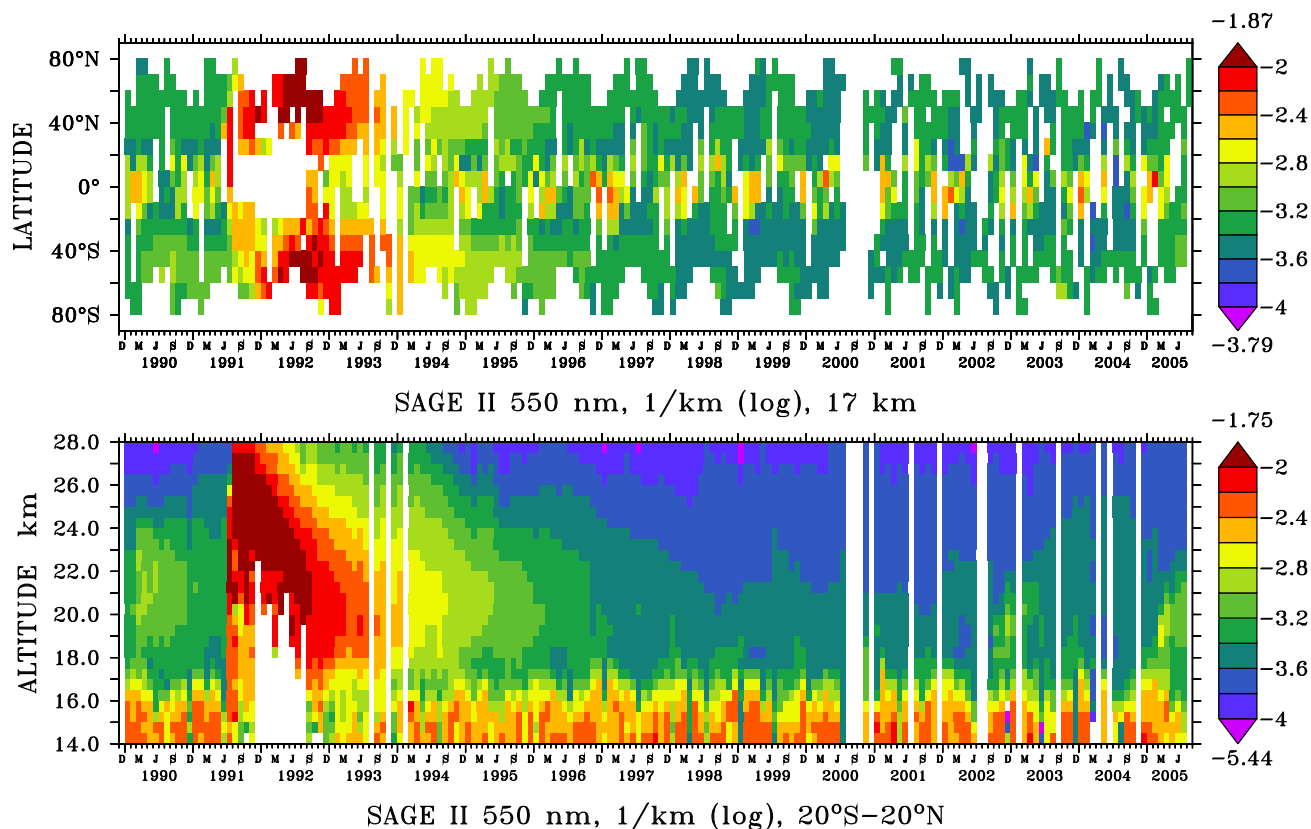
Figure 5. The logarithm of the extinction coefficient (1/km) of the SAGE II instrument from Thomason et al. (2008). The dataset spans the period January 1990–August 2005: Horizontal distribution at 17 km altitude (top) and vertical distribution for tropical regions 20° S–20° N (bottom). Maximum and minimum values appear above (dark red) and below (violet) the colour keys, respectively. White: no data.

The uncertainty of the operational SAD product during background periods is affected by several parameters, including the
lack of sensitivity to particles with radii smaller than 100 nm, the number of degrees of freedom indicated by the averaging
kernels of the aerosol extinction at different wavelength channels and the temperature profile used in the data processing
(Thomason et al., 2008). The uncertainty also depends by the altitude and is <35 % between 12 km and 18 km, <25 % between
18 km and 30 km and 50 % at altitudes above 30 km (Bingen et al., 2003). After the large eruption of Mount Pinatubo in 1991,
"saturation" effects at lower altitudes were observed in the profiles for more than one year, meaning that the aerosol load was
so high that the light signal received by the instrument was below the limit of detection. This effect corresponds to the large
white areas for 1991 and 1992 in Figure 5. Red pixels around 14–16 km correspond to measurements contaminated by clouds,
increasing the optical depth in the upper troposphere/lower stratosphere (UTLS) region on the lower panel of Figure 5. The
perturbations by convective clouds occur mostly over the West Pacific and were excluded in the procedure for estimating the
SO$_2$ injections. The data gaps in the year 2000 were caused by an instrument failure causing SAGE II to be switched off for
several months.

3 Description of the setup for the EMAC Model

The computations for this study were performed on the Mistral supercomputer at the Deutsches Klimarechenzentrum (DKRZ), Hamburg, Germany. For this purpose, EMAC (ECHAM5/MESSy Atmospheric Chemistry), a coupled atmospheric circulation model consisting of the 5th generation of European Centre Hamburg general circulation model (ECHAM5) and the Modular Earth Submodel System (MESSy) was used. The model simulations performed in the period from 2002 to 2012 by the global atmospheric chemistry climate model EMAC in Bingen et al. (2017) and Brühl et al. (2018) were extended to 1990 to 2019 in this study.

3.1 The ECHAM5 General Circulation Model

ECHAM5 (5th generation of European Centre Hamburg general circulation model) is an atmospheric general circulation model (Roeckner et al., 2003, 2006), which runs with self-consistent quasi-biennial oscillation (QBO). It is nudged to the meteorological ERA-Interim reanalysis data of the European Centre for Medium-Range Weather Forecasts (ECMWF) up to about 100 hPa. As we here focused on the stratosphere, the middle atmosphere version L90 with 90 layers up to 0.01 hPa (~80 km) and high vertical resolution in the lower stratosphere was needed (Giorgetta et al., 2006). For these model simulations, the horizontal resolution T63 (1.87° × 1.87°) was chosen.

3.2 The Modular Earth Submodel System (MESSy)

MESSy (Modular Earth Submodel System) is an earth system model, which consists of several submodels (Jöckel et al., 2005, 2006, 2010). An overview of the submodels used in this study is given in Table A1 in the appendix.

The convection was calculated with the CONVECT submodel (Tost et al., 2006b), with the convection scheme from Tiedtke (1989) and the Nordeng (1994) closure. The convection parametrization is sensitive to the model resolution, which results in differences between different model resolutions in the vertical transport of tracers, like dust and water vapor or ozone (Brühl et al., 2018). To avoid a phase drift, we used the QBO submodel for weak nudging to the QBO zonal wind observations (Giorgetta et al., 2002).

The plumes of outgasing volcanic SO_2 emissions (Diehl et al., 2012) are imported via the OFFEMIS submodel as 3-D field volume emission fluxes (Kerkweg et al., 2006b), while mineral dust emissions are calculated online using the emission scheme of Astitha et al. (2012) as part of the ONEMIS submodel. The exchange of dimethyl sulfide (DMS) between the air-sea interface of the ocean and the atmosphere is simulated by the AIRSEA submodel (Pozzer et al., 2006).

The gas- and aqueous-phase chemistry in the troposphere and stratosphere is calculated interactively with the CAABA/MECCA (Chemistry As A Boxmodel Application/Module Efficiently Calculating the Chemistry of the Atmosphere) submodel (Sander et al., 2011). Specifically, the chemically generated SO_2 is calculated from fluxes of sulfate precursor gases and further transformed to H_2SO_4 (Brühl et al., 2018). The chemistry of the CAABA/MECCA submodel contains photolysis reactions, which need photolysis rate coefficients (J-values) for tropospheric and stratospheric species computed by the JVAL submodel.

CAABA/MECCA is also coupled to the Multiphase Stratospheric Box Model (MSBM) for heterogeneous reactions on aerosols and Polar Stratospheric Clouds (PSCs) (Jöckel et al., 2010) to allow for feedback on ozone.

For parametrisation of aerosol microphysical processes, we used the Global Modal-aerosol eXtension (GMXe) aerosol module (Kerkweg, 2005; Stier et al., 2005; Vignati et al., 2004) and we described aerosol species using several interacting lognormal aerosol modes, specifically four soluble and three insoluble modes. The original mode boundaries of the aerosol size distribution from Pringle et al. (2010) were adapted for this setup to volcanic aerosol conditions in the stratosphere as shown in Table 1 to avoid overly rapid sedimentation of coarse aerosol particles after big volcanic eruptions.

Mode boundaries	Pringle et al. (2010)	σ	Brühl et al. (2018)	σ
Nucleation mode: soluble	$<10\,\text{nm}$	1.69	$1\,\text{nm}$–$12\,\text{nm}$	1.59
Aitken modes: soluble & insoluble	$10\,\text{nm}$–$100\,\text{nm}$	1.69	$12\,\text{nm}$–$140\,\text{nm}$	1.59
Accumulation modes: soluble & insoluble	$100\,\text{nm}$–$1\,\mu\text{m}$	1.69	$140\,\text{nm}$–$3.2\,\mu\text{m}$	1.49
Coarse modes: soluble & insoluble	$>1\,\mu\text{m}$	2.2	$>3.2\,\mu\text{m}$	1.7

Table 1. Diameters of aerosol mode boundaries in the GMXe submodel for tropospheric (Pringle et al., 2010) and volcanic stratosphere conditions (Brühl et al., 2018), including the corresponding mode distribution width (σ).

The nucleation of new particles consists only of completely soluble sulfate aerosols and is calculated by the parametrisation used by Vehkamäki et al. (2002). Further, the evaporation of liquid sulfate particles back to the gas phase in the middle stratosphere is possible in the model. The loss of gas phase species to the aerosol is parametrized in the 3rd EQuilibrium Simplified Aerosol Model (EQSAM3) (Metzger and Lelieveld, 2007). The uptake of gases on wet particles and on acid aerosol particles is included in the model calculation. Calculated sulfate is used by MSBM for heterogeneous chemistry. Furthermore, the AERosol OPTical properties in the model are calculated online with the AEROPT submodel (Dietmüller et al., 2016) and are coupled to the GMXe submodel. The resulting extinction coefficient is given at wavelengths of 350, 550, 750 and 1025 nm for comparison with GOMOS, OSIRIS and SAGE. Finally, the parameters from AEROPT are used in the radiation scheme as input for the radiative transfer calculations and to calculate the AOD.

The influence of stratospheric aerosol on radiative forcing and heating is calculated online for diagnostic purposes. Via multiple calls of the RAD submodel, the forcing is simulated with stratospheric aerosol above 100 hPa only and without any aerosol (Brühl et al., 2012). The RAD_FUBRAD sub-submodel is used to calculate the shortwave heating rates from the absorption of UV by O_2 and O_3 in the upper stratosphere and mesosphere. The lowermost level of the RAD_FUBRAD sub-submodel for the upper atmosphere is shifted from above 70 hPa in the original version of Dietmüller et al. (2016) to 30 hPa–14 hPa to allow for scattering by the aerosol in the simulations with volcanic emissions.

Concerning removal mechanisms, the SCAVenging submodel calculates the loss of atmospheric tracers and aerosols by wet deposition, as well as the liquid phase chemistry in clouds and precipitation (Tost et al., 2006a). The uptake and oxidation of tracers is considered for both liquid and mixed phase clouds, also including the aqueous sulfur oxidation of SO_2 to SO_4^{2-}.

4 Generation of a Volcanic Sulfur Emission Inventory

In a previous inventory of volcanic eruptions based on SO_2 vertical profiles from MIPAS, we estimated the aerosol radiative forcing from 2002 to 2011 by simulating the evolution of SO_2 in the atmosphere reported by Brühl et al. (2015) and by

230 improving the resulting time series using aerosol measurements from Bingen et al. (2017). The results of these simulations showed that significant discrepancies remained with respect to radiative forcing estimated from measurements (Brühl et al., 2018). In this work, we further improve the volcanic sulfur emission inventory by analysing additional satellite data sets and by including all identified relevant eruptions between 1990 and 2019. The result is presented in Table 2 and provides the injection time into the model, the coordinates of the ejected plume and the amount of emitted SO_2. Each volcano is identified

235 by its name if available, and by the concerned region if the name is unknown. Geological information is received from the "Global Volcanism Program, Smithsonian Institution" (https://volcano.si.edu/). An appropriate comparison of SO_2 mixing ratio measurements from MIPAS and of the aerosol extinction from GOMOS requires consideration of a time shift of about two weeks as a result of the particle formation from the gas phase. As mentioned above, the SAGE II dataset is used to extend the time series to the period preceding ENVISAT's launch, while OSIRIS is used for the period after ENVISAT.

240 The amount of sulfur emitted by each single eruption is calculated by integration of SO_2 vertical profiles from MIPAS observations (Höpfner et al., 2015), excluding tropospheric emissions below 12 km at high latitudes, 13 km at mid-latitudes, and 14 km at low latitudes. The altitudes and latitudes indicated in the table correspond to the locations of the maximum SO_2 mixing ratios of the volcanic plumes. The longitudes refer to the locations of the volcanoes, because the plumes have been moved by the zonal winds during the time lag between eruption and observation. In the cases of OSIRIS, SAGE and GOMOS

245 this shift can easily be 100 degrees. When comparing the SO_2 emissions reported here with those of Carn et al. (2016), it should be noted that Carn et al. (2016) makes use of total SO_2 emissions, including rapidly removed tropospheric SO_2, while the present study only takes into account the long-lived, climate-relevant stratospheric fraction of the emitted SO_2.

It should be noted as well that the date of the volcanic eruption can differ by a few days from the date of injection in the model simulation, because the temporal resolution of the data sets is about five days at least (or weeks in the SAGE period). In some

250 cases, more than one eruption is found in the same time step within an interval of five days. In such a case, all eruptions are listed in the same line. The integration time has to be extended for data gaps, which increases the uncertainty and complicates the identification of the right volcano. In such a case, the name of the most probable volcano is tagged with a "?". If the SO_2 emissions of two volcanoes cannot be separated with certainty, both are indicated with a "+" in the same line. This uncertainty is frequent in the Republic of Vanuatu, an island country located in one of the most volcanically active regions in the South

255 Pacific, referred to as "Vanuatu" in Table 2.

Volcano or region	Time	Latitude (°)	Longitude (°)	Altitude (km)	SO$_2$ (kt)	Instrument
Kelut	11 Feb 1990	-8	112	16, 22	410	S
Gamalama	25 Apr 1990	0	127	16	96	S
Raung (?)	25 Jul 1990	-8	115	16	63	S

Volcano or region	Time	Latitude (°)	Longitude (°)	Altitude (km)	SO$_2$ (kt)	Instrument
Pacaya +	16 Sep 1990	15	-90	16	10	S
Sabancaya	6 Oct 1990	-16	-7	17	75	S
Papua +	12 Jan 1991	-4	145	17	88	S
Fernandina	20 Apr 1991	0	-92	16	118	S
Pinatubo	16 Jun 1991	15	120	23	16942	S
Hudson	10 Aug 1991	-46	-73	18	1276	S
Cerro Negro	10 Apr 1992	12	-87	22	18	S
Spurr	28 Jun 1992	61	-152	17	291	S
Spurr	19 Aug 1992	61	-152	16, 18	298	S
Spurr	18 Sep 1992	61	-152	17	187	S
Lascar	18 Apr 1993	-23	-68	22	376	S
Langila, Galeras (?)	30 Oct 1993	-5, 1	145, -70	17	50	S
Yasur?	17 Mar 1994	-16	165	16	80	S
Rinjani, Nyamuragira, Central America	6 Jul 1994	-8, -1, 12	117, 30, -90	16	63	S
Rabaul	20 Sep 1994	-4	150	18-22	89	S
Merapi, Ecuador	23 Nov 1994	-7, 1	110, -70	17, 17	48, 57	S
Peru, Africa, Vanuatu	15 Feb 1995	-15, -1, -15	-78, 30, 168	17, 16, 16	7, 43, 25	S
Mexico + Soufriere Hills	10 Aug 1995	16	-98, -62	16	81	S
Peru + Colombia, Rabaul	10 Feb 1996	-15, 5, -4	-80, -80, 150	17, 16, 16	65, 96	S
Soufriere Hills	26 May 1996	16	-62	16	53	S
Soufriere Hills + Mexico, Rabaul	18 Sep 1996	16, -4	-62, -98, 150	16	59, 28	S
Nyamuragira, Manam	3 Dec 1996	-1, -5	30, 145	17	45, 90	S
Manam + Langila	11 Feb 1997	-5	145	17	107	S
Popocatepetl	1 Jul 1997	19	-98	16	32	S
Soufriere Hills, Philippines	20 Oct 1997	16	-62	15, 16	36, 20	S
Soufriere Hills, Papua	26 Dec 1997	16	-62, 150	16	37, 22	S
Tungurahua (?), Vanuatu	2 Feb 1998	-1, -16	-78, 168	17, 16	98, 15	S
Soufriere Hills	4 Jul 1998	16	-62	16	56	S
Manam, Cerro Azul, Nyamuragira	7 Oct 1998	-5, 0, -1	144, -90, 30	17, 17, 16	28, 39, 19	S
Guagua Pinch + Tungurahua, Vanuatu	23 Jan 1999	-1, -16	-78, 165	17, 16	75, 49	S
Cameroon	31 Mar 1999	4	10	16	63	S
Mayon, Colombia	22 Jun 1999	13, 2	124, -80	17, 16	41, 46	S
Soufriere Hills +	24 Jul 1999	16	-62	17	42	S
Ulawun, Tungurahua + Guagua Pichincha	16 Nov 1999	-5, -1	150, -78	17	31, 51	S
Vanuatu, Nyamuragira, Tungurahua	4 Feb 2000	-16, -1, 0	165, 30, -78	17, 16, 16	33, 41, 12	S
Mayon + Vanuatu, Tungurahua	29 Feb 2000	13, -16, -1	124, 168, -78	16, 16, 16	25, 32	S

Volcano or region	Time	Latitude (°)	Longitude (°)	Altitude (km)	SO$_2$ (kt)	Instrument
Ulawun (+ Miyakejima)	26 Sep 2000	-5	150	17	42	S
Nyamuragira, Mayon(?)	13 Feb 2001	-1, 13	30, 124	16, 18	47, 88	S
Ulawun	29 Apr 2001	-5	150	16	41	S
Mayon, Lopevi	23 Jun 2001	13, -16	124, 168	16, 16	49, 22	S
Tungurahua, Soufriere Hills	7 Aug 2001	0, 16	-78, -62	16, 16	29, 46	S
Africa, Tungurahua +	25 Sep 2001	-1, 0	30, -78	16	31, 47	S
Tungurahua (+ Manam), Nyiragongo	14 Jan 2002	-5, -1	-78(144), 30	17, 15	83, 19	S
Tungurahua (+ Africa)	20 Mar 2002	-1	-78 (30)	17	77	S
Nyamuragira	23 Jul 2002	-1	30	15	23	M
Witori	2 Aug 2002	-6	150	14	18	M
Ruang	26 Sep 2002	2	125	18	71	M, G
El Reventador	5 Nov 2002	0	-78	17	77	M, G
Nyiragongo, Lokon	9 Jan 2003	-1, 1	30, 125	15, 16	12, 10	M, G
Nyiargongo, Lokon (Rabaul?)	5 Mar 2003	-5, 1	30, 125	17, 15	12, 13	M, G
Anatahan, Nyiaragongo, Ulawun	14 May 2003	16, -1, -5	143, 30, 150	16, 16, 17	9, 15, 6	M
Lewotobi, Kanlaon	13 Jun 2003	-8, 10	123, 123	15, 15	9, 15	M, G
Soufriere Hills	13 Jul 2003	16	-62	17	41	M, G
Gamalama, Japan	17 Aug 2003	1, 33	128, 131	16, 16	8, 7	M, G
Bezymianny or Klyuchevskoy	6 Sep 2003	56	160	14	8	G
Lokon, Soufriere Hills + Masaya	26 Sep 2003	2, 15	125, -62	16, 16	7, 5	M, G
Rabaul	10 Nov 2003	-5	150	16	17	M, G
Rabaul	5 Dec 2003	-5	150	16	13	M, G
Rabaul, Nyiaragongo?	9 Jan 2004	-5, -1	150, 30	17, 15	11, 9	M, G
Langila, Nyiaragongo?	3 Feb 2004	-5, -1	150, 30	17, 17	11, 3	M, G
Soufriere Hills	4 Mar 2004	10	-62	17	22	M, G
Nyamuragira, Awu + Tengger	12 Jun 2004	-1, 4, -8	30, 125, 112	17, 15	20, 18	G
Pacaya, Galeras	17 Jul 2004	15, 1	-91, -77	17, 17	11, 11	G
Galeras	11 Aug 2004	1	-77	16	15	G
Vanuatu, Rinjani + Kerinci	30 Sep 2004	-16, -8, -2	168, 116, 101	15, 15, 17	7, 15	G
Manam, Soputan	30 Oct 2004	-4, 1	144, 125	16, 16	8, 11	G
Manam, Nyiragongo	24 Nov 2004	-4, -1	144, 30	17, 15	18, 11	G
Nyiaragongo, Reventador	4 Dec 2004	0, 0	30, -77	16, 16	19, 5	G
Vanuatu, Soputan	24 Dec 2004	-16, 1	168, 125	17, 15	15, 16	G
Manam	28 Jan 2005	-4	144	18	130	M, G
Anatahan, (+)	3 Apr 2005	16	143	15	15	M
Anatahan, Soufriere Hills	23 Apr 2005	16, 16	143, -62	16, 16	21, 21	M

Volcano or region	Time	Latitude (°)	Longitude (°)	Altitude (km)	SO$_2$ (kt)	Instrument
Anatahan, Fernadina, Vanuatu	18 May 2005	16, 0, -16	143, -91, 168	15, 15, 15	8, 11, 6	M
Anatahan, Santa Ana	12 Jun 2005	16, 14	143, -90	15, 15	12, 9	M
Anatahan, Soufriere Hills	12 Jul 2005	16, 16	143, -62	15, 15	14, 10	M
Anatahan, Raung	6 Aug 2005	16, -8	143, 113	15, 15	13, 20	M
Anatahan, Raung	16 Aug 2005	16, -8	143, 113	15, 15	14, 17	M, G
Santa Ana	5 Oct 2005	14	-90	17	32	M
Sierra Negra, Dabbahu	25 Oct 2005	-1, -13	-91, 40	15, 15	16, 22	G
Karthala, Galeras	24 Nov 2005	-10, -2	43, -80	16, 16	13, 11	M, G
Soputan, Lopevi	24 Dec 2005	1, -16	125, 168	16, 16	23, 13	M, G
Rabaul +	23 Jan 2006	-5	152	16	25	G
Manam, Chile	4 Mar 2006	-5, -40	144, -70	17, 16	58, 6	G, T
Cleveland	14 Mar 2006	53	-170	13	8	G
Ecuador, Tinakula, Lascar	18 Apr 2006	-5, -10, -23	-78, 166, -68	17, 17, 17	13, 17, 3	M
Soufriere Hills	23 May 2006	16	-62	19	125	M, G, T
Kanlaon	2 Jul 2006	10	123	20	42	M
Tungurahua, Rabaul	16 Aug 2006	-2, -4	-78, 150	19, 17	40, 20	M, G, T
Rabaul	10 Oct 2006	-4	150	17	131	M, T
Ubinas, Vanuatu	25 Oct 2006	-20, -20	-70, 168	17, 15	8, 25	M
Ambrym	9 Nov 2006	-10	160	17	27	M, T
Nyamuragira, Mexico	29 Nov 2006	5, 5	30, -90	17, 15	28, 21	M, G, T
Bulusan, Soputan, Vanuatu	24 Dec 2006	13, 1, -16	125, 125, 168	18, 16, 15	8, 8, 14	M, G
Karthala, Bulusan, Lascar, Shiveluch, Vanuatu	23 Jan 2007	-10, 13, -23, 57, -16	43, 125, -68, 160, 168	17, 17, 15, 15, 15	5, 5, 6, 7, 5	M, G, T
Nevado del Huila, Karthala, Vanuatu	22 Feb 2007	0, -10, -16	-70, 43, 168	16, 15, 16	8, 10, 8	M, G, T
Etna, Reventador, Ambrym	24 Mar 2007	38, 0, -16	15, -78, 160	15, 16, 17	8, 17, 14	M, G, T
Piton de la Fournaise, Reventador +	8 Apr 2007	-20, 0	57, -80	16, 16	22, 11	M, G, T
Ulawun, Vanuatu, Nevado del Huila	3 May 2007	-5, -25, 3	150, 160, -70	15, 15, 15	11, 5, 6	M, G, T
Papua, Kamchatka, Nyamuragira, Ubinas + Lascar	13 May 2007	-10, 50, 0, -20	150, 150, 30, -75	16, 16, 16, 16	6, 1, 10, 6	M, G
Llaima, Vanuatu, Bulusan	23 May 2007	-30, -15, 13	-70, 160, 125	18, 15, 17	10, 6, 7	M, G
Soputan, Bezymianny, Telica	12 Jun 2007	1, 56, 13	125, 160, -87	16, 14, 15	13, 7, 9	M, G
Lengai, Mexico	2 Jul 2007	2, 20	29, -90	16, 15	14, 9	M
Raung, Japan (+)	27 Jul 2007	-5, 35	110, 130	15, 15	10, 10	M
Manda Hararo, Java	11 Aug 2007	12, -5	40, 115	17, 15	13, 14	M, T
Vanuatu, Mexico	20 Sep 2007	-5, 20	180, -90	16, 16	8, 13	M
Jebel al Tair, Galeras	5 Oct 2007	16, 1	42, -80	16, 16	41, 8	M, T

Volcano or region	Time	Latitude (°)	Longitude (°)	Altitude (km)	SO$_2$ (kt)	Instrument
Galeras, Jebel al Tair, Soputan	4 Nov 2007	-2, 15, -5	-80, 42, 110	16, 16, 16	7, 5, 8	M, G
Soputan or Krakatau, Galeras, Chikurachki	14 Nov 2007	-5, -1, 50	110, -75, 155	16, 16, 15	9, 8, 10	M
Talang, Galeras	9 Dec 2007	0, 0	100, -75	16, 16	10, 12	M
Ulawun?	19 Dec 2007	1	150	17	17	M, G
Nevado del Huila, Llaima	3 Jan 2008	1, -35	-75, -71	17, 15	26, 4	M
Galeras, Anatahan	23 Jan 2008	-3, 15	-80, 145	16, 16	14, 7	M
Tungurahua, Papua	12 Feb 2008	-5, -5	-80, 155	16, 17	13, 10	M
Batu Tara (+)	13 Mar 2008	-5	125	16	26	M, G
Lengai, Andes, Kerinic	28 Mar 2008	-5, 5, -2	36, -80, 101	16, 16, 16	6, 4, 7	M
Egon, Nevado del Huila	12 Apr 2008	-5, 5	122, -76	15, 17	14, 9	M
Mexico, Ibu, Chaiten	27 Apr 2008	15, -35	-90, 125 -70	16, 16, 16	9, 11, 3	M
Mexico, Barren Island, Chaiten	12 May 2008	10, 10, -35	-90, 90, -70	14, 16, 14	10, 14, 5	M
Soputan, Nicaragua/Costa Rica	16 Jun 2008	1, 1	125, -85	16, 16	26, 8	M
Okmok, Soputan	21 Jul 2008	53, 1	-168, 125	16, 16	51, 27	M
Kasatochi	15 Aug 2008	52	-175	17	273	M, G
Dallafilla, Nevado del Huila, Reventador	13 Nov 2008	14, 3	40, -78	17, 17	39, 28	M
Karangetang, Galeras, Japan	18 Dec 2008	3, 0, 30	125, -80, 130	17, 17, 15	15, 10, 9	M, G
Barren Island, Galeras	2 Jan 2009	10, 3	90, -80	17, 15	10, 10	M
Indonesia?, Galeras	27 Jan 2009	-5, 0	100, -80	16, 16	12, 10	M
Galeras, Villarrica, Karangetang, Vanuatu	16 Feb 2009	-2, -35, 3,-16	-78, -75,100,168	16, 15, 16, 17	11, 6, 6, 7	M
Redoubt, Galeras	28 Mar 2009	60, 0	-155, -75	13, 15	61, 43	M
Fernandina, Nyamuragira	12 Apr 2009	0, 0	-90, 30	16, 16	12, 16	M
Galeras + Reventador	7 May 2009	0	-75	15	25	M
Rinjani, Vanuatu, Reventador	22 May 2009	-5, -15, 3	116, 165, -80	16, 16, 16	4, 4, 13	M
Sarychev, Manda Hararo	21 Jun 2009	48, 12	153, 40	16, 16	446, 82	M, G
Vanuatu, Mayon, Galeras	4 Oct 2009	-15, 13, 2	165, 120, -80	17, 17, 17	4, 6, 10	M
Tungurahua, Hawaii, Vanuatu	19 Oct 2009	5, 20, - 16	-76, -155, 165	16, 16, 16	7, 5, 5	M, G
Galeras, Karkar, Vanuatu	3 Dec 2009	0, -5, -16	-78, 146, 165	17, 17, 17	12, 10, 4	M
Mayon, Nyamuragira, Vanuatu	2 Jan 2010	13, 0, -15	120, 30, 168	16, 16, 16	8, 8, 9	M
Turrialba, Vanuatu	17 Jan 2010	5, -15	-82, 168	16, 16	9, 9	M
Soufriere Hills	16 Feb 2010	16	-62	17	36	M
Arenal, Indonesia, Vanuatu	2 Apr 2010	9, 0, -16	-84, 120, 168	15, 15, 15	14, 12, 5	M
Tungurahua, Dukono, Vanuatu	2 May 2010	-5, 2, -16	-78, 128, 168	16, 16, 16	14, 10, 7	M
Pacaya, Ulawun, Sarigan	6 Jun 2010	15, -5, 16	-91, 150, 145	17, 16, 15	27, 6, 4	M
Ulawun, Costa Rica, Miyakejima	16 Jul 2010	-5, 15, 35	150, -87, 140	16, 16, 16	8, 13, 6	M, G
Karangetang, Nicaragua, Vanuatu	15 Aug 2010	3, 15, -16	125, -85, 168	16, 16, 16	12, 12, 6	M

Volcano or region	Time	Latitude (°)	Longitude (°)	Altitude (km)	SO$_2$ (kt)	Instrument
Galeras, Sinabung	30 Aug 2010	5, 5	-77, 100	16, 16	10, 12	M
Karangetang, Barren Island	4 Oct 2010	3, 12	125, 94	16, 16	20, 13	M
Merapi	8 Nov 2010	-7	110	17	97	M
Tengger, Tungurahua, Chile	23 Dec 2010	-8, -3, -40	110, -78, -75	17, 17, 17	16, 13, 8	M
Tengger	7 Jan 2011	-8	110	16	24	M
Lokon, Planchon, Bulusan	26 Feb 2011	1, -35, 13	125, -75, 125	16, 15, 16	13, 4, 12	M
Karangrtang, Sangay, Planchon	23 Mar 2011	2, -2, -35	125, -78, -75	15, 15, 15	10, 10, 5	M
Galeras?, Karangetang	12 Apr 2011	5, 5	-77, 128	16, 16	10, 9	M
Tungurahua, Dukono, Vanuatu	2 May 2011	2, 2, -16	-78, 128, 160	16, 16, 15	13, 9, 5	M
Grimsvötn, Lokon	27 May 2011	65, 1	-20, 125	14, 16	18, 27	M
Puyehue	11 Jun 2011	-41	-71	13	23	G
Nabro	21 Jun 2011	13	41	18	406	M, G
Soputan, Marapi	20 Aug 2011	1, 0	125, 100	18, 16	9, 3	M, G
Manam, Tungurahua	19 Oct 2011	-4, -3	144, -78	16, 16	8, 8	M
Nyamuragira	18 Nov 2011	-2	29	16	31	M
Gamalama, Nyamuragira	18 Dec 2011	1, -1	128, 29	16, 15	19, 13	M
Vanuatu, Nyamuragira	12 Jan 2012	-16, -1	168, 29	16, 14	14, 12	M
Vanuatu, Nyamuragira	11 Feb 2012	-16, -1	168, 29	17, 17	16, 15	M
Nevado del Ruiz, Marapi	12 Mar 2012	-3, 0	-76, 100	16, 17	12, 15	M
Nyamuragira, Mexico	7 Jun 2012	-1, 20	29, -95	16, 15	30, 4	O
Soputan, Nevado del Ruiz, Mexico	27 Aug 2012	1, 5, 20	124,-76,-95	16, 16, 15	30, 15, 5	O
Nyamuragira, Mexico, Peru	14 Oct 2012	-1, 20, -20	29, -95, -70	16, 16, 15	40, 15, 10	O
Nyamuragira, Paluweh, Nevado del Ruizz	7 Nov 2012	-1, -8, 5	29, 122, -76	15, 16, 17	20, 30, 17	O
Copahue, Lokon +	22 Dec 2012	-38, 1	-71, 125	15, 17	10, 45	O
Paluweh, Karkar	3 Feb 2013	-8, -5	122, 145	16, 17	25, 22	O
Karkar, Vanuatu (+?)	10 Mar 2013	-5, -16	145, 168	17, 16	24, 20	O
Rabaul, Nevado del Ruiz, Nyamuragira	18 Apr 2013	-3, 5, -1	150,-76, 29	17, 17, 16	40, 9, 20	O
Mayon, Turrialba, Pavlof	8 May 2013	13, 10, 55	124, -84, -162	17, 16, 14	35, 24, 6	O
Rabaul, Mexico	10 Jul 2013	-3, 20	150, -95	16, 15	30, 15	O
Pacaya	15 Aug 2013	15	-91	16	43	O
Sinabung, Ubinas	15 Sep 2013	3, -16	98, -71	17, 15	35, 8	O
Merapi, Nyamuragira, Pacaya	18 Nov 2013	-7, -1, 15	110, 29, -91	17, 17, 15	30, 13, 8	O
Sinabung, Nyamuragira	9 Dec 2013	3, -1	98, 29	17, 16	26, 15	O
Sinabung +	11 Jan 2014	3	98	16	29	O
Kelut	15 Feb 2014	-8	112	20	170	O
Merapi, Tungurahua	27 Mar 2014	-7, -1	110, -78	16, 16	31, 33	O

Volcano or region	Time	Latitude (°)	Longitude (°)	Altitude (km)	SO$_2$ (kt)	Instrument
Santa Maria, Semeru	9 May 2014	15, -8	-91, 113	16	25, 39	O
Sangeaang-Api	31 May 2014	-8	119	17	60	O
Nyamuragira, Pavlof, Fuego, Dukono (Tungurahua)	9 Jul 2014	-1, 55, 14, 2	29, -162, -91, 128	16, 15, 15, 16	20, 10, 12, 20	O
Rabaul, Fuego	29 Aug 2014	-3, 14	150, -91	16, 16	36, 20	O
Nyamuragira	11 Sep 2014	-1	29	15	30	O
Ontakesan	27 Sep 2014	36	137	17	34	O
Sinabung, Turrialba	23 Oct 2014	3, 10	98, -84	17, 16	34, 17	O
Fogo, Semeru, Ubinas	24 Nov 2014	15, -8, -16	-24, 113, -71	17, 17, 16	11, 33, 11	O
Nevado del Ruiz, Nyamuragira, Vanuatu	16 Dec 2014	5, -1, -16	-76, 29, 168	15, 17, 16	8, 12, 21	O
Nyamuragira, Vanuatu, Honga Tonga	14 Jan 2015	-1, -16, -21	29, 168, -175	16, 16, 15	21, 17, 13	O
Vanuatu, Nyamuragira, Soputan	16 Feb 2015	-16, -1, 1	168, 29, 124	17, 16, 16	13, 13, 13	O
Soputan, Nevado del Ruiz, Santa Maria, Villarrica	8 Mar 2015	1, 5, 15, -39	125,-76,-91,-72	17, 16, 15, 15	14, 14, 8, 5	O
Tungurahua?, Batu Tara?	5 Apr 2015	-1, -8	-78, 124	17, 17	17, 22	O
Calbuco	25 Apr 2015	-41	-73	18	292	O
Manam, Tungurahua?	8 May 2015	-4, -1	144, -78	17, 17	24, 25	O
Wolf, Aira + Kuchinoerabujima	26 May 2015	0, 32, 30	-91, 131, 130	16, 15	63, 20	O
Raung	4 Jul 2015	-5	110	17	27	O
Cotopaxi, Raung, Suwanosjima, Manam	14 Aug 2015	0, -5, 30, -4	-80,110,130,144	16, 16, 16, 20	24,18,10,16	O
Nev.Ruiz + Reventador, Fuego, Sumatra	21 Sep 2015	5, 14, 3	-76, -91, 98	16, 17, 16	13, 8, 19	O
Sinabung, Fuego, Cotopaxi, Copahue	15 Oct 2015	3, 14, 0, -38	98, -91, -80, -71	16, 17, 15, 15	30, 15, 6, 13	O
Lascar, Sinabung, Nyamuragira, Fuego	30 Oct 2015	-23, 3, -1, 14	-70, 98, 29, -91	17, 17, 16, 16	13,17,12,17	O
Vanuatu, Tungurahua, Telica, Rinjani	17 Nov 2015	-16, -1,13, -5	168,-78,-87,116	18, 17, 17, 16	18,20,10,18	O
Vanuatu, Reventador, Tengger	5 Dec 2015	-16, 0, 2	168, -78, 120	17, 16, 16	16, 15, 12	O
Reventador, Sinabung	18 Dec 2015	0, 3	-78, 100	17, 16	16, 16	O
Soputan +, Reventador, Fuego	8 Jan 2016	1, 0, 14	125, -78, -91	16, 17, 14	25, 19, 5	O
Semeru, Fuego	10 Feb 2016	-8, 14	113, -91	17, 16	34, 25	O
Vanuatu +, Tungurahua	27 Feb 2016	-16, -1	168, -78	16, 16	24, 16	O
Tungurahua, Sinabung +, Pavlof	15 Mar 2016	-1, 3, 55	-78, 98, -162	16, 17, 15	23, 26, 7	O
Reventador, Sinabung +, Fuego, Aira	13 Apr 2016	0, 3, 14, 32	-78, 98, -91, 131	17, 16, 15, 15	18, 30, 17, 6	O
Fuego, Nyamuragira + Ecuador, Langila, Sinabung	7 May 2016	14, -1, -5, 3	-91, 29, 150, 98	16, 17, 16, 17	16, 18, 16, 26	O
Bulusan, Sinabung, Semeru, Mexico	10 Jun 2016	13, 3, 8, 15	125,98,113,-100	17, 16, 17, 16	16,14,16,10	O
Rinjani, Sinabung, Santa Maria	1 Aug 2016	-5, 3, 15	116, 98, -91	16, 16, 16	10, 30, 24	O
Sinabung + Vanuatu, Fuego	28 Aug 2016	-16, 14	168, -91	16, 16	42, 23	O

Volcano or region	Time	Latitude (°)	Longitude (°)	Altitude (km)	SO$_2$ (kt)	Instrument
Ubinas, Sinabung	3 Oct 2016	-16, 3	-71, 98	15, 16	16, 26	O
Sabancaya, Sinabung + Bulusan	5 Nov 2016	-16, 3	-72, 98	16, 16	38, 46	O
Dukono, Vanuatu, Sabancaya	12 Dec 2016	2, -16, -16	128, 168, -72	17, 18, 15	30, 28, 28	O
Sabancaya,Reventador,Sinabung+Vanuatu	10 Jan 2017	-16, 0, 3	-72, -78, 98	16, 17, 17	20, 30, 23	O
Sabancaya, Colima, Sinabung	4 Feb 2017	-16, 19, 3	-72, -104, 98	15, 16, 16	17, 15, 25	O
Sabancaya, Dukono, Fuego, Manam + Vanuatu, Bogoslof, Nevados de Chillán	5 Mar 2017	-16, 2, 14, -16, 53, -37	-72, 128, -91, 168, -170, -71	16, 17, 17, 17, 15, 15	10, 18, 8, 28, 4, 5	O
Sabancaya, Nevado del Ruiz, Sinabung, Vanuatu, Klyuchevskoy	10 Apr 2017	-16, 5, 3, -16, 56	-72, -75, 98, 168, 160	16, 16, 16, 16, 15	8, 15, 19, 17, 2	O
Sinabung, Manam, Fuego	5 May 2017	3, -4, 14	98, 145, -91	16, 17, 17	26, 10, 19	O
Sheveluch + Bogoslof	19 May 2017	57	161	15	20	O
Santa Maria, Sheveluch +, Manam	16 Jun 2017	15, 57, -4	-91, 161, 145	16, 16, 15	11, 33, 6	O
Fuego, Sinabung +, Sheveluch +	5 Jul 2017	14, 3, 57	-91, 98, 161	15, 16, 15	22, 21, 4	O
Sinabung, Cristobal + Fuego, Sheveluch + Bogoslof	8 Aug 2017	3, 13, 54	98, -87, -168	16, 17, 16 (26?)	31, 27, 5	O
Tinakula, Ambae	21 Oct 2017	-10, -15	166, 168	15, 15	60	O
Agung, Ambae, Sabancaya	27 Nov 2017	-8, -15, -5	116, 168, -80	15, 16, 15	22, 7, 12	O
Mayon, Vanuatu, Sabancaya	22 Jan 2018	13, -15, -5	124, 168, -80	15, 17, 16	7, 20, 16	O
Fuego, Vanuatu	1 Feb 2018	14, -15	-91, 168	16, 16	20, 17	O
Sinabung, Vanuatu	19 Feb 2018	3, -15	98, 168	16, 16	14, 21	O
Ambae, Vanuatu	26 Mar 2018	-15	168	16	60	O
Ambae	6 Apr 2018	-15	168	17	91	O
Sabancaya	15 May 2018	-16	-72	16	16	O, T
Fuego	3 Jun 2018	14	-91	16	15	O, T
Fernandina	17 Jun 2018	0	-92	15	8	T
Agung, Sabancaya	28 Jun 2018	-8, -16	115, -72	17, 16	33, 23	O, T
Sierra Negra	8 Jul 2018	-1	-92	15	25	T
Ambae	20 Jul 2018	-15	168	17	228	O, T
Manam, Sabancaya	25 Aug 2018	-3, -16	144, -72	17, 16	25, 12	O, T
Krakatau, Sabancaya	23 Sep 2018	-6, -16	105, -72	16, 16	5, 11	O
Manam, Soputan, Reventador+Sangay	4 Oct 2018	-3, 1, 0	144, 125, -78	16, 16, 16	7, 4, 22	O
Nev.Ruiz, Sabancaya	24 Oct 2018	5, -16	-75, -72	16, 16	22, 11	O
Fuego, Sabancaya, Krakatau	6 Nov 2018	14, -16, -6	-91, -72, 105	16, 16, 15	10, 16, 19	O
Fuego, Sabancaya, Bagana	26 Nov 2018	14, -16, -6	-91, -72, 155	16, 16, 16	8, 9, 12	O
Saban., Manam, Soputan, Vanuatu	8 Dec 2018	-16, -3, 1,-16	-72,144,125,168	16, 17, 16, 15	24, 8, 4, 6	O

Volcano or region	Time	Latitude (°)	Longitude (°)	Altitude (km)	SO$_2$ (kt)	Instrument
Krakatau, Vanuatu, Sabancaya	23 Dec 2018	-6, -16, -16	105, 168, -72	16, 15, 16	7, 6, 20	O
Krakatau, Sabancay, Manam	4 Jan 2019	-6, -16, -3	105, -72, 144	17, 17, 16	5, 20, 9	O
Manam, Sabancaya	24 Jan 2019	-3, -16	144, -72	17, 16	23, 14	O
Manam, Sabancaya	14 Feb 2019	-3, -16	144, -72	16, 16	12, 13	O
Manam, Sabancaya, Mexico, Chile	19 Mar 2019	-3,-16,18,-24	144,-72,-98,-68	17, 16, 18, 15	9, 12, 6, 7	O
Sabancaya., Manam, N.Ruiz, Gamalama	20 Apr 2019	-16, -3, 5, 1	-72, 144,-75,128	17, 16, 16, 16	31, 12, 15, 7	O, T
Sinabung, Manam, Sabancaya	25 May 2019	3, -3, -16	98, 144, -72	17, 16, 16	11, 20, 21	O, T
Raikoke	22 Jun 2019	48	153	17	196	O
Raikoke, Ulawun	29 Jun 2019	48, -5	153, 151	15, 19	221, 107	O, T
Ubinas, Raikoke, Manam	19 Jul 2019	-16, 48, -3	-71, 153, 144	15, 16, 17	72, 141, 15	O, T
Ulawun, Mexico	3 Aug 2019	-5, 20	151, -100	19, 17	111, 12	O
Ubinas	16 Aug 2019	-16	-71	16	27	O, T

Table 2: Volcanic Sulfur Emission Inventory of volcanic SO$_2$ emissions into the stratosphere integrated above 14 km in low latitudes, 13 km in mid-latitudes and 12 km in high latitudes. Derived from satellite data (2002–2012), by MIPAS **(M)** and updated on the basis of GOMOS **(G)** and TOMS/OMI/OMPS **(T)**. Based on a previous study from Brühl et al. (2018) with scaling factors for T63 and already published in an earlier version in Bingen et al. (2017). Extended with satellite data from SAGE II(V7.00) **(S)** back to 1990–2002, and from 2012–2019 by OSIRIS **(O)**. For detailed description see the text.

5   Implementation of SO$_2$ from the Volcanic Sulfur Emission Inventory into the EMAC Model

The amount of SO$_2$ injected from each volcanic eruption is calculated by integrating the vertical SO$_2$ profiles, described in Table 2. Then, the SO$_2$ plumes are incorporated into the model simulations by adding the satellite-derived 3-dimensional perturbations of SO$_2$ mixing ratios to the simulated SO$_2$ at the time of the eruptions. In order to get the correct altitude distribution and to reduce additional errors caused by the low temporal resolution of the satellite data, we did not implement the volcanic SO$_2$ emissions as point sources. In addition, effusive eruptions and quiescent degassing volcanoes from the time-dependent monthly climatology of Diehl et al. (2012) were added to the tropospheric SO$_2$ background emissions in the model simulations and truncated at an altitude of 200 hPa to avoid double counting in the stratosphere and uppermost troposphere (Brühl et al., 2018).

The SO$_2$ emissions of the volcanic sulfur emission inventory are used in the EMAC model simulations, resulting in the time series shown in Figure 6, with mixing ratios between background conditions of a minimum of 0.001 ppb$_v$ (parts per billion by volume (10^{-9})) in volcanically quiescent periods, and highly active volcanic conditions with a maximum of 114 ppb$_v$ (as indicated at the top of the colour key, 5-day average) after the Pinatubo eruption. In the Junge-aerosol layer, typical mixing ratios of SO$_2$ are about 0.03 ppb$_v$.
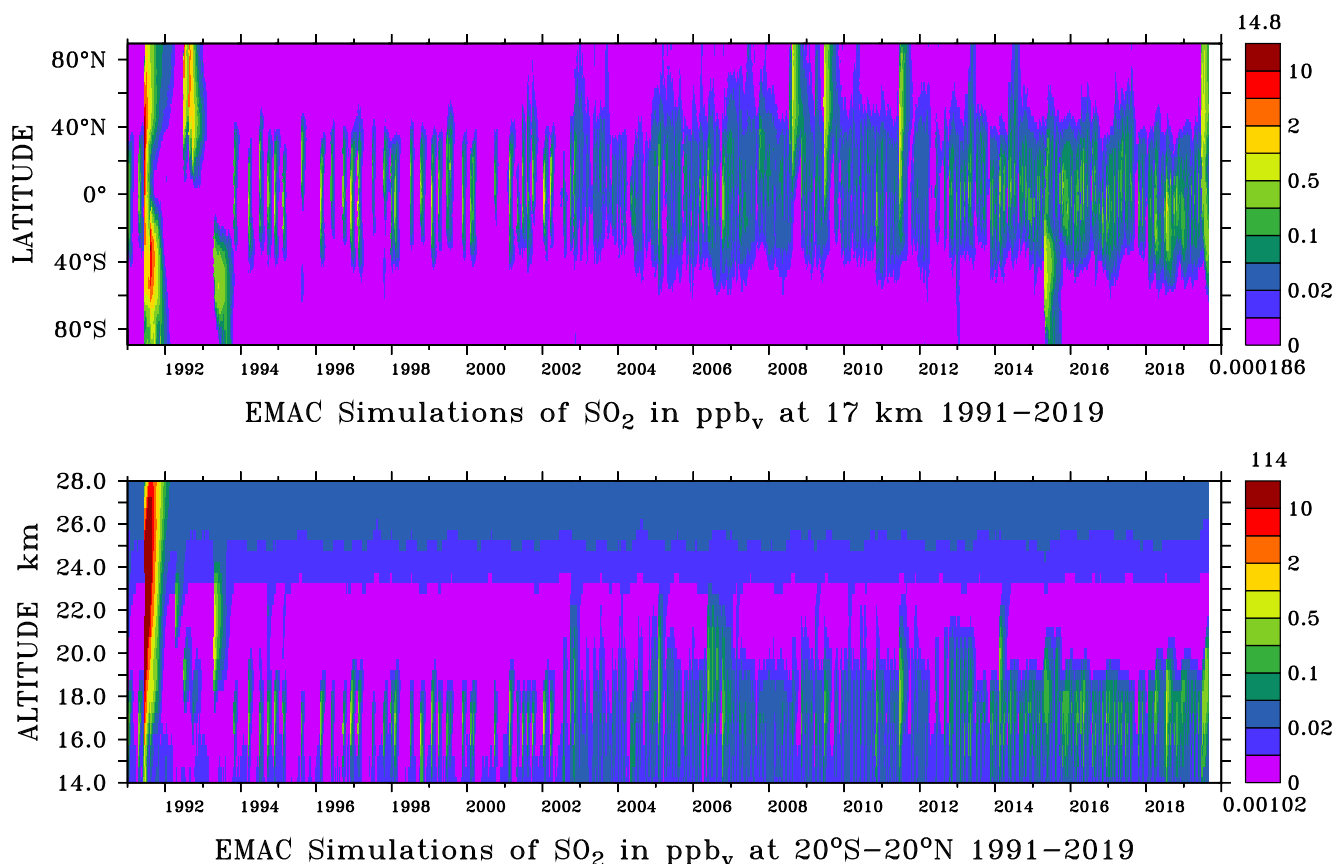
Figure 6. EMAC simulation of the stratospheric SO_2 mixing ratios (ppb_v) (January 1991–August 2019) from the volcanic sulfur emission inventory (Table 2), in horizontal T63 resolution at 17 km altitude (top) and in vertical distribution for tropical regions $20°$ S–$20°$ N (bottom). Maximum and minimum values are indicated above (dark red) and below (violet) the colour keys, respectively.

270   The volcanic eruptions in 1990 are entered into the model during the spin-up phase of the model simulations (not shown), with the emissions of the first entry in Table 2 set to the upper limit. The low number of volcanic eruptions in 1991 and the following years is due to the low coverage of satellite data and "saturation" effects of the satellite instrument (See subsection 2.4 about SAGE). The signatures of medium and small volcanic eruptions are too weak to be seen during the high concentrations in the first years after the Pinatubo eruption. From 2002 onwards, a higher number of small volcanic eruptions is captured in

275   the volcanic sulfur emission inventory. This is rather due to the improved data coverage enabled by a larger number of satellite instruments, than to higher volcanic activity.

In most cases, the stratospheric SO_2 mixing ratios are highest at tropical latitudes. For this reason, tropical regions ($20°$ S–$20°$ N) are chosen for the vertical distribution in the lower illustration of Figure 6 and subsequent figures. Exceptions to this typical SO_2 pattern are single strong volcanic eruptions at high latitudes like Kasatochi (2008), Sarychev (2009) and Raikoke

280   (2019) in the northern hemisphere or Calbuco (2015) in the southern hemisphere. Another noteworthy case is the Nabro

(2011) eruption, where the volcanic emissions were transported from the tropics to northern latitudes by the Asian monsoon circulation.

MIPAS typically captures background SO_2 mixing ratios in the lowermost tropical stratosphere at 16 km to 17 km of around $0.02\,ppb_v$ to $0.05\,ppb_v$ (Figure 1), which can be reproduced by the model only if many more volcanoes are considered than

285   listed in the National Aeronautics and Space Administration (NASA) SO_2 database (Brühl et al., 2015). Some time periods with low volcanic activity resulting in stratospheric background conditions can be identified between 1996 and 2004. To reach realistic SO_2 mixing ratios in the lower tropical stratosphere during these years, the oxidation of DMS and other sulfur species is needed. The lower panel of Figure 6 shows increasing SO_2 with altitudes of above 23 km due to additional production from OCS photolysis.

290   The comparison of the simulated and observed SO_2 values shows that the volcanic SO_2 emissions from the volcanic sulfur emission inventory in Table 2 correlate well with the peaks of the mixing ratios in Figure 6, as they dominate the stratospheric sulfur burden. In the stratosphere, SO_2 is converted to sulfate aerosol, which explains most of the interannual variability of the stratospheric aerosol burden as well as its influence on the stratospheric radiation. Generally, the conversion from SO_2 to sulfate aerosol particles takes about two weeks in the UTLS and about two months in the lower and middle stratosphere.

295   Enhanced SO_2 concentrations from Pinatubo via photolysis of gaseous H_2SO_4 remained in the mesosphere for several years (Brühl et al., 2015).

6   Climate impact of stratospheric aerosol in EMAC model simulations

We compared the global influence of sulfur emissions on different atmospheric optical parameters. Based on Mie-theory-lookup tables, optical properties such as optical depths, single scattering albedos and asymmetry factors, which are used in radiative

300   transfer simulations, were calculated online for different aerosol types: sulfate, dust, organic carbon and black carbon, sea salt, and aerosol water. Via multiple calls of the radiation module RAD with and without aerosol the influence of stratospheric aerosol on instantaneous radiative forcing and heating is computed online (subsection 3.2). Also, the feedback to atmospheric dynamics is included.

6.1   EMAC model simulations of the stratospheric aerosol extinction

305   Figure 7 and Figure 8 show the global stratospheric aerosol extinction coefficients (in decadal logarithm) for the period 1991— 2019 at 550 nm and 750 nm wavelengths of the EMAC model simulations at 17 km altitude and its vertical profile for tropical regions for 20° S–20° N. For medium eruptions, the maximum of the aerosol extinction lies at an altitude between 16 km and 18 km. For this reason, an altitude of 17 km is chosen in the following analyses.

The EMAC model simulations of the aerosol extinction coefficients at 550 nm (Figure 7) agree well with the satellite mea-

310   surements of GOMOS (Figure 2) and SAGE II (Figure 5) for the aerosol layer at an altitude of 16–22 km where measured extinction values exceed $\approx 2\times 10^{-4}\,km^{-1}$. The strongest event in these model simulations is the Pinatubo (Table 2) eruption in 1991, which dominates the stratospheric aerosol extinction coefficient for more than three years after the eruption with a global
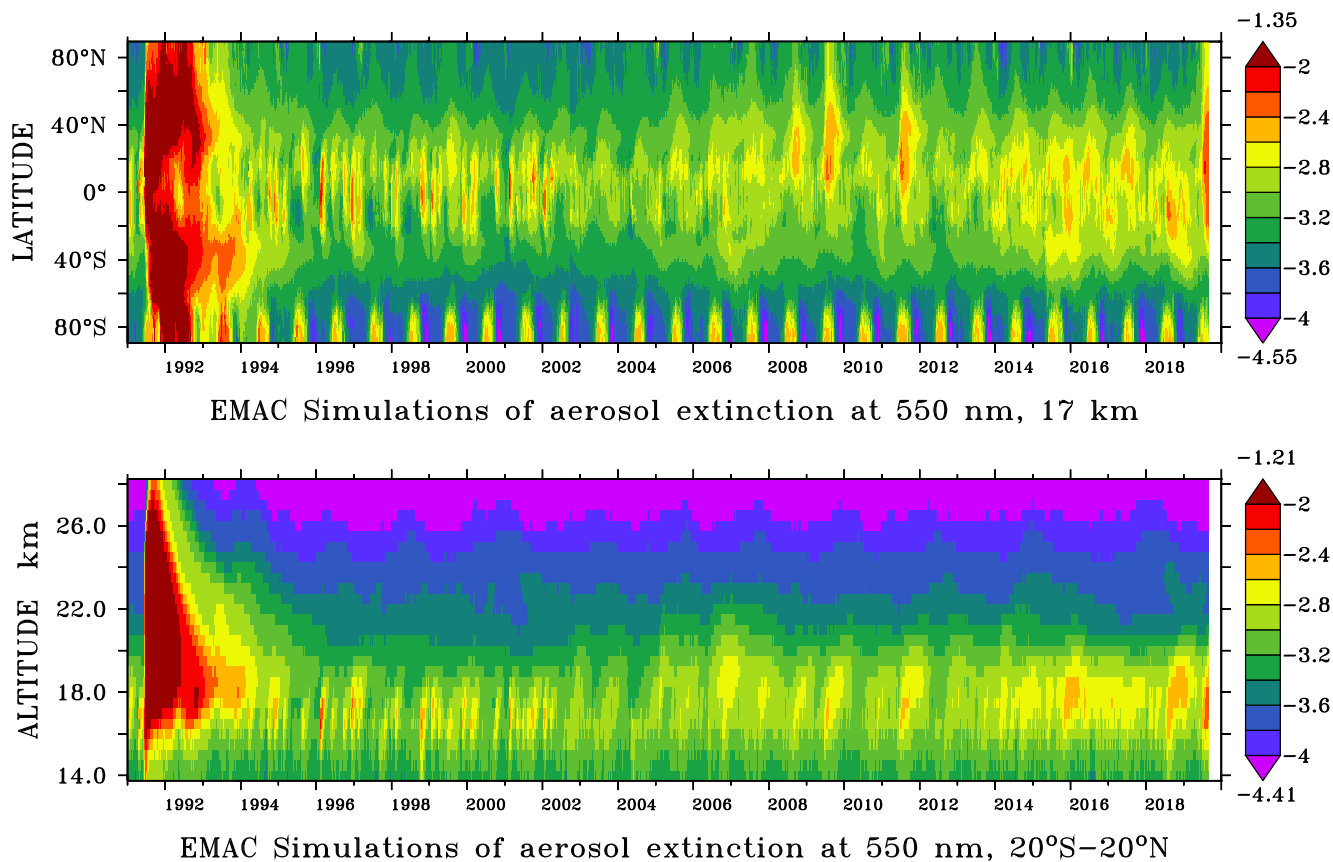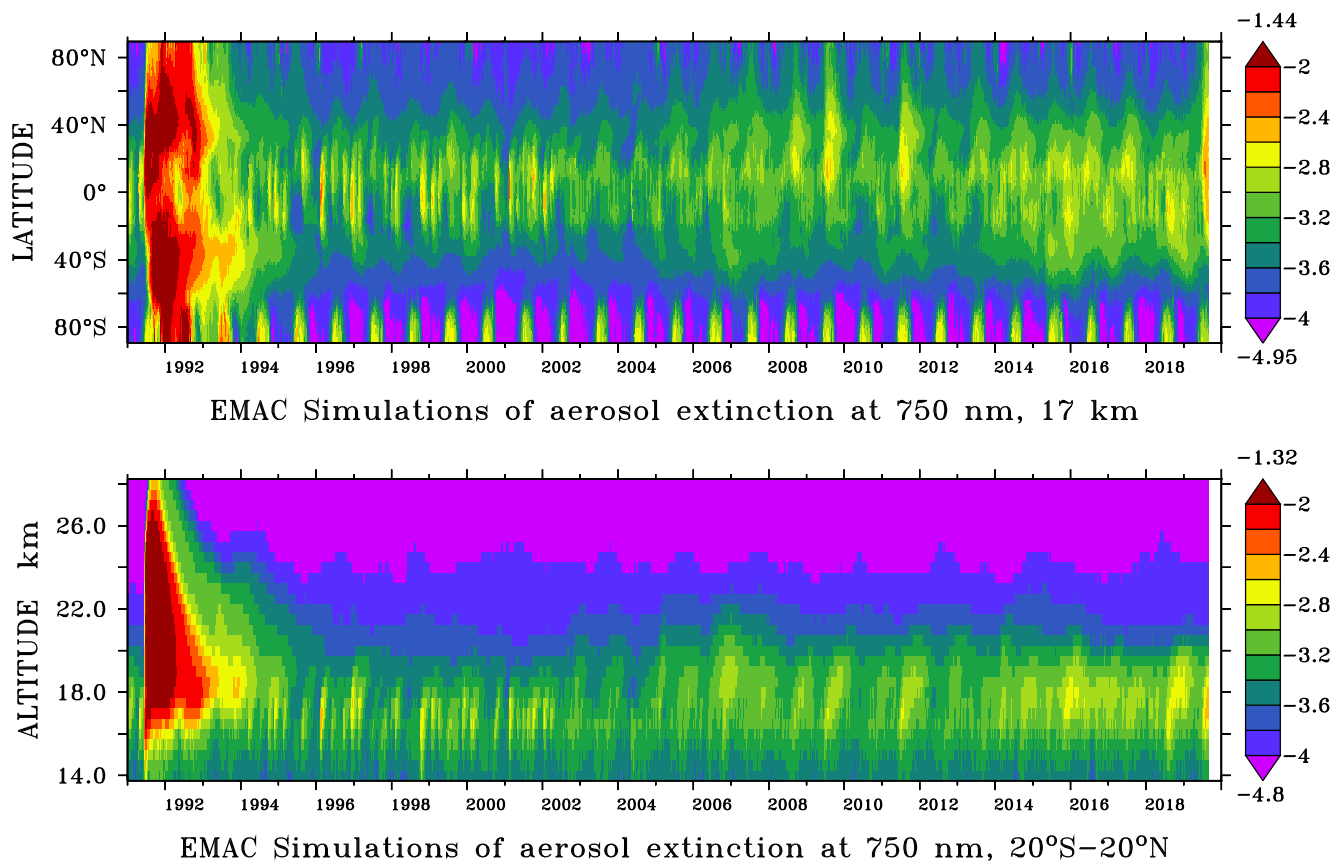
Figure 7. EMAC simulation of the stratospheric aerosol extinction in logarithmic scale log(1/km) for 550 nm wavelength from January 1991–August 2019 based on the volcanic sulfur emission inventory (Table 2), in horizontal T63 resolution of zonal mean at 17 km altitude (top) and in vertical distribution for tropical regions 20° S–20° N (bottom). Maximum and minimum values appear above (dark red) and below (violet) the colour keys, respectively.

distribution from the equator to the poles in both hemispheres and a maximum altitude of more than 26 km. All other eruptions are significantly smaller, and for this reason a logarithmic scale is chosen.

315   The model simulations of the aerosol extinction coefficient at 750 nm wavelength are required for the comparison with GOMOS (Figure 3) and OSIRIS (Figure 4). The two figures show a similar distribution of the aerosol extinction at wavelengths of 550 nm and 750 nm. Due to the typical size and composition of stratospheric aerosol particles, the aerosol extinction is higher at 550 nm than at 750 nm. The peaks caused by mineral dust particles during summer in the Northern subtropics are more pronounced at 750 nm than at 550 nm.

320   Despite the presence of volcanoes in Antarctic (like Mount Erebus), the seasonal change of extinction coefficient is not due to volcanic eruptions, but to the presence of Polar Stratospheric Clouds (PSCs) as simulated by the model.

Figure 8. EMAC simulation of the stratospheric aerosol extinction in logarithmic scale log(1/km) for 750 nm wavelength from January 1991–August 2019 based on the volcanic sulfur emission inventory (Table 2), in horizontal T63 resolution of zonal mean at 17 km altitude (top) and in vertical distribution for tropical regions 20° S–20° N (bottom). Maximum and minimum values appear above (dark red) and below (violet) the colour keys, respectively.

6.2   EMAC model simulations comparing the Aerosol Optical Depth (AOD)

The total stratospheric Aerosol Optical Depth (AOD) is obtained by the vertical integral of the aerosol extinction above an altitude of about 16 km (for mid-latitudes above about 14 km). The stratospheric AOD is shown on a logarithmic scale in

325   Figure 9 and Figure 10 with the new model simulations (red line) compared to satellite observations (light blue, green, and blue lines). Unlike most other studies, the stratospheric AOD is compared at the original wavelengths derived from different optical channels of the satellite instrument measurements. This avoids introducing additional errors through the use of conversion factors to adjust the values between the different wavelengths.

From 1991 to 2012, SAGE II (light blue line), GOMOS (green line) and SAGE+CALIPSO and SAGE+OSIRIS (blue line)

330   provide satellite data at a wavelength of 550 nm (Figure 9, OSIRIS data were converted from 750 nm by Glantz et al. (2014)).
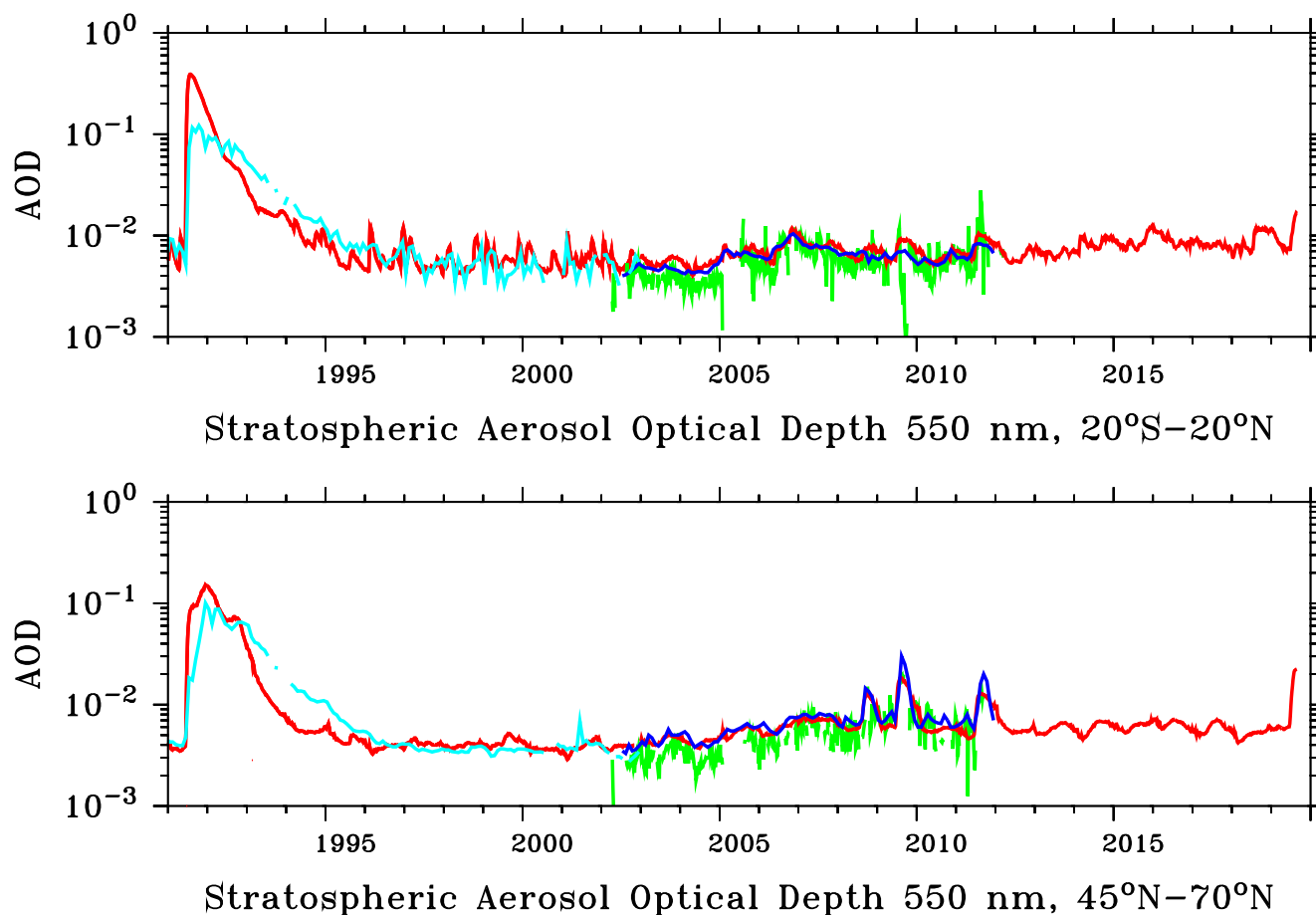
Figure 9. The stratospheric Aerosol Optical Depth at 550 nm wavelength for tropical regions 20° S–20° N above 110 hPa is shown on the top and for the northern hemisphere 45° N–70° N above 145 hPa at the bottom. Satellite observations from SAGE II (Thomason et al., 2008) are indicated by the light blue line, GOMOS (Bingen et al., 2017) by the green line and values derived from SAGE+CALIPSO (upper figure) (Santer et al., 2014) and SAGE+OSIRIS (lower figure) (Glantz et al., 2014) by the blue line. The red line shows the EMAC model simulations using the SO_2 injections of Table 2.

The maximum is reached after the Pinatubo eruption with a stratospheric AOD of 0.4 being an order of magnitude larger than the following medium eruptions with a stratospheric AOD of about 0.01 (e.g. Manam in early 1997, Rabaul in 2006 and Nabro in 2011). The differences after the large Pinatubo eruption in 1991 between the model simulations and the SAGE II observations are related to the "saturation" effects of the satellite instrument and can be observed for more than one year, (also shown above in Figure 5). Between 1993 and 1996 the reduction of the stratospheric AOD in the model simulations is faster than in the satellite observations. This indicates that the removal of stratospheric aerosol is still too fast from applying the modal model. Additionally, smaller volcanic eruptions might be missing, in view of the low number of identified events in the years after the Pinatubo eruption.

335
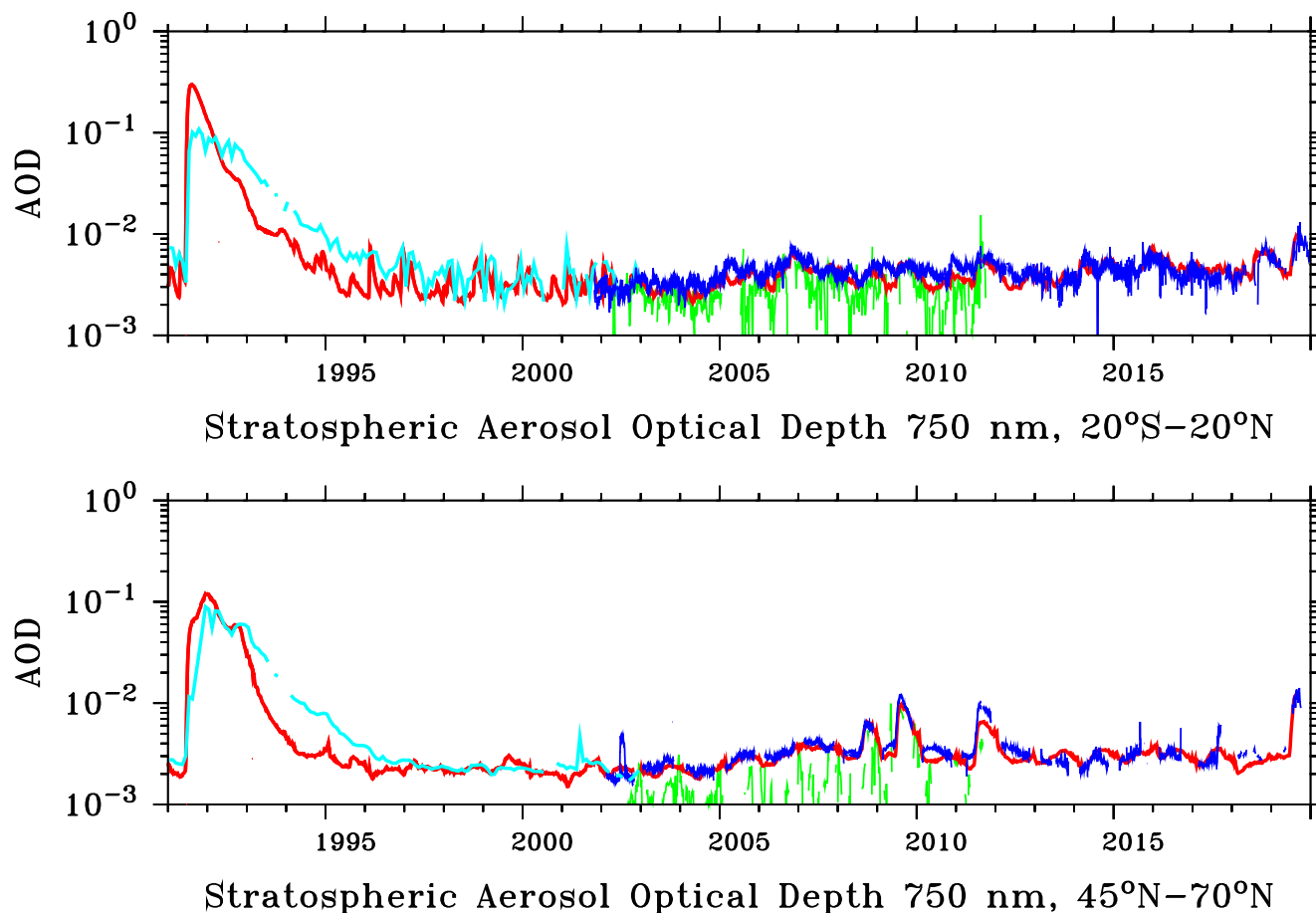
Figure 10. The stratospheric Aerosol Optical Depth at 750 nm wavelength for tropical regions 20° S–20° N above 110 hPa is shown on the top and for the northern hemisphere 45° N–70° N above 145 hPa at the bottom. Satellite observations from OSIRIS (Rieger et al., 2019) are indicated by the blue line and GOMOS (Bingen et al., 2017) by the green line. The light blue line shows the interpolation of SAGE data at 550 nm and 1025 nm wavelengths. The EMAC model simulations, using the SO_2 injections of Table 2, are shown by the red line.

In Figure 10, the coverage of GOMOS (green line) is often too low at a wavelength of 750 nm for the years from 2002 to 2012, so the inclusion of OSIRIS data (blue line) is important (Brühl et al., 2018). For the years after 2012 the timeline only contains data from OSIRIS at 750 nm wavelength.

The different distributions of the peaks in the upper and the lower figures is related to the latitude of the volcanic eruptions. Emissions reaching the stratosphere from strong eruptions in the tropics are distributed by the Brewer-Dobson circulation over the northern and southern hemisphere even to high latitudes, as in the cases of Soufriere Hills and Rabaul in 2006. However, if an eruption takes place at high latitudes (such as for Redoubt 2009) or at mid-latitudes like Kasatochi (2008) or Sarychev (2009), most of the emissions stay in the northern hemisphere and the signal in the tropics is weaker.

6.3 EMAC model simulations comparing the radiative forcing at the tropopause

The radiative forcing of the stratospheric aerosol is calculated by multiple calls of the RAD submodel (subsection 3.2). The simulated global negative radiative forcing in $\mathrm{Wm^{-2}}$ of stratospheric aerosol at the tropopause is illustrated in Figure 11.
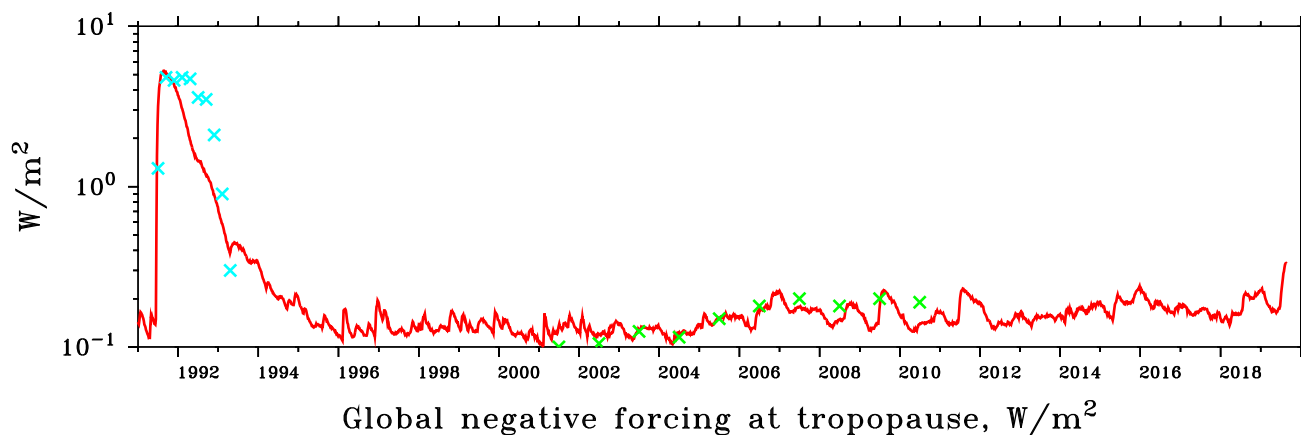
Figure 11. Global negative radiative forcing at the tropopause (185 hPa, solar + IR) by stratospheric aerosol. Estimated averages from satellite observations of the Earth Radiation Budget Experiment (ERBE) (Wong et al., 2006) are indicated by light blue crosses and annual averages derived from observations by Solomon et al. (2011) as green crosses. The EMAC model simulations with volcanic SO_2 are represented by the red line.

350   As the Pinatubo eruption caused a negative radiative forcing of more than a magnitude greater than all other eruptions since then, the y-axis is plotted in inverted logarithmic scale; for instance, 10^0 corresponds to a global negative radiative forcing of $1.0\,\mathrm{Wm^{-2}}$. The new model simulations with the additional volcanic eruptions (red line) are closer to the calculated estimates from satellite extinction measurements of SAGE, GOMOS and CALIOP (Cloud-Aerosol Lidar with Orthogonal Polarization) by Solomon et al. (2011) (green crosses) than in previous studies (e.g., Brühl et al. (2015)). This shows that even medium- and
355   small-sized volcanic eruptions can reach the stratosphere and have a significant influence on the global radiative forcing at the tropopause. In the period considered here, the volcanoes are the dominant factor in global negative radiative forcing, with up to $0.13\,\mathrm{Wm^{-2}}$ for Rabaul and Nabro and more than $0.2\,\mathrm{Wm^{-2}}$ for Raikoke/Ulawun compared to the volcanically quiescent period in 2002. Nevertheless, there remain small differences between the model simulation and the observations, for instance in 2010, which indicates missing volcanic eruptions (or an underestimation of the Merapi eruption by MIPAS). The strongest
360   global radiative forcing in the model simulations is caused by the Pinatubo eruption with a maximum of about -5 $\mathrm{Wm^{-2}}$; this is in good agreement with the results of Minnis et al. (1993). However, the same effect can be seen in Figure 11 as in Figure 9; that is, the maximum of the global negative radiative forcing drops again too quickly after the Pinatubo eruption. For the Pinatubo case, the particle fraction in the coarse mode is probably overestimated, resulting in an overestimation of sedimentation by large particles, even though the boundary between the accumulation and coarse modes in the aerosol module

365 GMXe was shifted from a diameter of 2.0 μm to 3.2 μm to represent stratospheric conditions with long residence times (Brühl et al., 2015).

6.4 EMAC model simulations of the stratospheric aerosol radiative heating

The simulated instantaneous aerosol radiative heating in the model is derived from multiple radiation calls with and without aerosol in the radiation submodel RAD. Aerosol formation is calculated by the GMXe submodel, while the aerosol optical
370 properties are calculated by the AEROPT submodel.
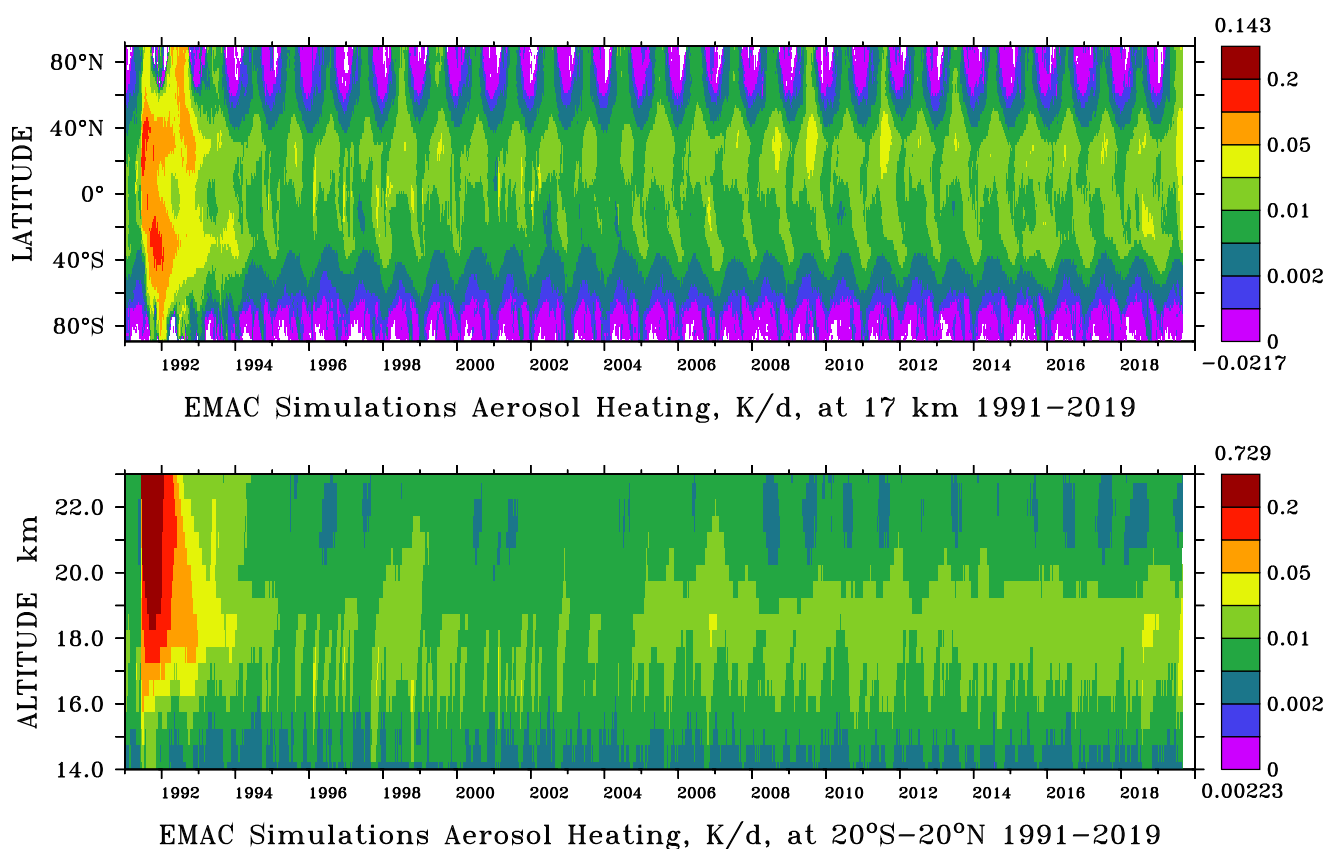
Figure 12. EMAC simulation of the aerosol radiative heating in K/day for solar and infrared radiation from January 1991–August 2019 based on the volcanic sulfur emission inventory (Table 2), in horizontal distribution at 17 km altitude (top) and in vertical distribution for tropical regions 20° S–20° N (bottom).

Figure 12 shows the calculated local heating effects in the stratospheric aerosol layer. Small and medium volcanic eruptions have the largest effects between altitudes of 17 km and 18 km and generate atmospheric heating of up to 0.03 K/day. The eruption of Pinatubo, on the other hand, had significantly stronger effects at altitudes of 20 km to 25 km and caused atmospheric heating of more than 0.7 K/day, which is about 23 times greater than all other eruptions in the model simulation, including 2019.

28

375   After such a strong volcanic eruption, the enhanced radiative heating exerts an effect on dynamics, influences the global spread
       of the volcanic cloud and leads to an upward transport of the aerosol itself as well as of other chemical tracers including ozone
       (Timmreck et al., 1999). Further, a seasonal signal contributes significantly to the radiative heating in the northern subtropics.
       This is caused by transport of desert dust to the UTLS mostly via the Asian summer monsoon convection, which generates
       additional heating during the time of the Asian summer monsoon (Brühl et al., 2018).

7   Discussion and conclusions

       The objective of this study was to generate a detailed volcanic sulfur emission inventory and to improve the EMAC model
       simulations of the global stratospheric aerosol and sulfate burden, and compute the volcano-induced radiative forcing through
       validation with satellite data.

       Compared to previous studies by Brühl et al. (2015) and Bingen et al. (2017), the horizontal resolution in these new model
385   simulations is increased from T42L90 to T63L90. Since the convection parametrisation of the model was developed for the
       higher resolution T63L90, the stratospheric aerosol distribution is also in much closer agreement with the satellite observations
       (section 2) than before (Brühl et al., 2018).

       Due to the newly available satellite data sets of SAGE II and OSIRIS, the time series could be extended in both directions
       to encompass a total of 29 years and now covers the years 1991 to 2019, instead of 2002 to 2012 in previous work. Additional
390   updated three-dimensional data sets are now available, which provide better temporal resolution than the monthly means of
       the MIPAS, GOMOS and OSIRIS instruments. The temporal resolution is now five days for the three instruments and it is
       possible to identify multiple volcanic eruptions within a short period of time. With the three-dimensional data sets, the vertical
       distribution of SO_2 can be distinguished and the amount of sulfur reaching the stratosphere can be calculated much more
       accurately than by estimation of a total column. To exclude tropospheric emissions and signals from high-altitude clouds, the
395   integration of the sulfur emissions is set above an altitude of 12 km at high latitudes, 13 km at mid-latitudes and 14 km at low
       latitudes. To avoid double counting, tropospheric sulfur emissions are treated separately.

       Our volcanic sulfur emission inventory is an improvement on the version published by Bingen et al. (2017). While the
       previous version included 230 explosive volcanic eruptions, the new version now lists more than 500 eruptions. An overview
       of these eruptions is given in the improved volcanic sulfur emission inventory in Table 2, which also includes the estimated
400   stratospheric SO_2 emissions as well as the plume altitudes. These consist of about 80 eruptions in the first time period between
       1990–2002 measured by the SAGE II instrument, 240 eruptions in 2002–2012 measured with multiple instruments and 230
       eruptions in the last time period 2012–2019 measured by OSIRIS. Older versions of the volcanic sulfur emission inventory did
       not incorporate enough data to allow assessment of the true volcanic contribution to the radiative forcing of the atmosphere
       and only spanned the period 2002–2012.
405   Strong volcanic eruptions can inject several teragrams of SO_2 directly into the stratosphere. For this reason, the maxima of
       the global stratospheric SO_2 concentrations correlate well with the eruption events of the volcanic sulfur emission inventory in
       Table 2.

The SO$_2$ emissions of smaller volcanic eruptions can reach the lower stratosphere by convective transport through the tropical tropopause, which results in accumulation of sulfate aerosol in the lower stratosphere. This was demonstrated to be

410 essential for correctly assessing the extinction coefficient in volcanically quiescent periods.

Our analysis shows the importance of using multi-instrument satellite data sets to fill data gaps and to detect as many volcanic eruptions as possible. The best data coverage was in the time period from 2002 to 2012, for which simultaneous measurements from the MIPAS, GOMOS and OSIRIS instruments are available. The evaluation by the satellite data sets shows that GOMOS is important for detecting volcanic eruptions in MIPAS data gaps and for a better attribution of individual

415 eruptions. Consequently, the combination of MIPAS, GOMOS and OSIRIS data leads to better SO$_2$ input and calculating the radiative forcing in the chemistry climate model EMAC.

Our work also confirms the importance of improving the volcanic sulfur emissions inventory for the modelling of the radiative effects by stratospheric aerosols. The new model simulations demonstrate that volcanic emissions have a dominant impact on the stratospheric aerosol burden and explain most of the interannual variability of the stratospheric aerosol extinction

420 during the considered time period. These emissions have a large impact on the stratospheric aerosol forcing and heating, which influence the climate and the global circulation for a few years after big volcanic eruptions.

The aerosol radiative heating resulting from large volcanic eruptions like Pinatubo triggers enhanced tropical upwelling, which causes a lofting of the injected SO$_2$ and the aerosol as well as other chemical tracers. Here, the radiative feedback on dynamics is required for estimates of the aerosol extinction in the upper part of the volcanic aerosol plume that correspond

425 with observations.

Big volcanic ash plumes can interfere with the SO$_2$ signal in satellite measurements, and satellites could be "blind" during the first few days or months after an eruption (Höpfner et al., 2015). However, most volcanic ash particles are relatively large and sediment after some hours or days, so they have only minor climatic significance (Boucher, 2015) and are not discussed in detail here. There are, however, volcanoes (e.g. Kelut, 2014) which emit small ash particles which can stay in the lower

430 stratosphere for several months (Vernier et al., 2016). Moreover, it has been found that the model setup might have to be improved by including an additional aerosol mode to slow down the removal by sedimentation of stratospheric aerosol after big volcanic eruptions.

Some satellite data sets still contain data gaps and noise. Comparing the model results with OSIRIS data in the northern tropics (Figure 10) indicates that some volcanic events are still underestimated or missing in the volcanic sulfur emission

435 inventory in the year 2010. This could also explain the differences between the model simulations and satellite observations, indicated by green crosses in Figure 11 of the radiative forcing in this year.

A study of Neely et al. (2011) shows that meteoric smoke is the dominant source of aerosol extinction in the upper stratosphere and mesosphere above 40 km in the tropics and above 35 km poleward of 30 degrees in latitude. The meteoric material could act as sink for gaseous H$_2$SO$_4$. Detected meteoric dust in the UTLS (Schneider et al., 2021) also suggests that it has to

440 be incorporated into the model to reproduce observations of higher aerosol concentrations in the upper stratosphere. Thus, the aerosol extinction for the upper stratosphere and mesosphere is underestimated in model simulations without implementation of meteoric material in the radiation calculations.

The model also includes mineral dust and organics from the troposphere transported up to the UTLS. The EMAC simulations show a seasonal signal in the stratospheric AOD and an enhanced radiative heating in the northern hemisphere, induced by the
445 convective transport of mineral dust to the UTLS in the Asian monsoon region. This is confirmed by satellite observations and studies by Klingmüller et al. (2018). The influence of wildfires and other biomass burning plumes on stratospheric AOD has increased in recent years (Fromm et al., 2019), and this effect should be included in the model.

In any case, the findings of the IPCC (2013) report are confirmed: frequent volcanic eruptions of moderate and small intensities, injecting sulfur gases to the upper troposphere and lower stratosphere, contribute significantly to the stratospheric aerosol
450 layer through accumulation. These cause a global negative radiative forcing of 0.12 (0.22 to 0.08) Wm^{-2} at the surface, like in the case of the volcanic eruptions of Soufriere Hills/Rabaul (2006), Nabro (2011) and the combination of the Sinabung, Wolf and Calbuco eruptions (2015) with a radiative forcing of up to $0.13\,Wm^{-2}$, and $0.2\,Wm^{-2}$ for Raikoke/Ulawun (2019). This shows that also medium-sized volcanic eruptions can contribute to a slowdown of global warming like in the mid-2000s, thus improving the new model simulations, especially in 2007, a year for which several eruptions were not represented in previous
455 studies.

Author contributions. JS, CBr and JL defined the scientific questions and scope of this work. JS and CBr conceived the idea and methodology
465 used in this paper and carried out the model simulations and the analysis. MH provided the MIPAS data, CBi provided the GOMOS data and LR provided the OSIRIS data. All authors participated in the scientific discussion in regard to satellite data in particular. JS wrote the manuscript, and all authors reviewed the manuscript and provided advice on the manuscript and figures.

Competing interests. The authors declare that they have no conflicts of interest.

Atmospheric
Chemistry
and Physics
Discussions

Appendix A: List of MESSy submodels used in this study

Submodel	Function	Reference
AEROPT	Aerosol optical depth	Dietmüller et al. (2016)
AIRSEA	Air-sea exchange of trace gases	Pozzer et al. (2006)
CAABA/MECCA	Atmospheric chemistry	Sander et al. (2011)
CONVECT	Convection processes	Tost et al. (2006b)
CVTRANS	Convection transport of tracers	Tost et al. (2010)
DDEP	Dry deposition	Kerkweg et al. (2006a)
GMXe	Global Modal Aerosol eXtension	Pringle et al. (2010)
IMPORT	Import of external data files	Jöckel et al. (2006)
JVAL	Photolysis rate coefficients	Jöckel et al. (2006)
LNOX	NOx lighting production	Tost et al. (2007)
MSBM	Multiphase Stratospheric Box Model	Jöckel et al. (2010)
OFFEMIS	Off-line emissions	Kerkweg et al. (2006b)
ONEMIS	On-line emissions	Kerkweg et al. (2006b)
QBO	QBO nudging	Giorgetta et al. (2002)
RAD	RADiation	Dietmüller et al. (2016)
SCAV	Scavenging (wet removal)	Tost et al. (2006a)
SEDI	Aerosol sedimentation	Kerkweg et al. (2006a)
TNUDGE	Tracer nudging	Kerkweg et al. (2006b)
TROPOP	Tropopause calculation	Jöckel et al. (2006)

Table A1. List of used MESSy submodels. Reference and short description from http://www.messy-interface.org. Parts of the base model copied into MESSy which must always be active are not listed here.

Atmospheric
Chemistry
and Physics
Discussions

References

480 Astitha, M., Lelieveld, J., Abdel Kader, M., Pozzer, A., and De Meij, A.: Parameterization of dust emissions in the global atmospheric chemistry-climate model EMAC: Impact of nudging and soil properties, Atmospheric Chemistry and Physics, 12, 11 057–11 083, https://doi.org/10.5194/acp-12-11057-2012, 2012.

Bertaux, J. L., Kyrölä, E., Fussen, D., Hauchecorne, A., Dalaudier, F., Sofieva, V., Tamminen, J., Vanhellemont, F., Fanton d'Andon, O., Barrot, G., Mangin, A., Blanot, L., Lebrun, J. C., Pérot, K., Fehr, T., Saavedra, L., Leppelmeier, G. W., and Fraisse, R.: Global ozone
485 monitoring by occultation of stars: an overview of GOMOS measurements on ENVISAT, Atmospheric Chemistry and Physics, 10, 12 091–12 148, https://doi.org/10.5194/acp-10-12091-2010, 2010.

Bingen, C., Vanhellemont, F., and Fussen, D.: A new regularized inversion method for the retrieval of stratospheric aerosol size distributions applied to 16 years of SAGE II data (1984-2000): Method, results and validation, Annales Geophysicae, 21, 797–804, https://doi.org/10.5194/angeo-21-797-2003, 2003.

490 Bingen, C., Robert, C. E., Stebel, K., Brühl, C., Schallock, J., Vanhellemont, F., Mateshvili, N., Höpfner, M., Trickl, T., Barnes, J. E., Jumelet, J., Vernier, J.-P., Popp, T., de Leeuw, G., and Pinnock, S.: Stratospheric aerosol data records for the climate change initiative: Development, validation and application to chemistry-climate modelling, Remote Sensing of Environment, 203, 296–321, https://doi.org/10.1016/j.rse.2017.06.002, 2017.

Bingen, C., Robert, C., Hermans, C., Vanhellemont, F., Mateshvili, N., Dekemper, E., and Fussen, D.: A Revised Cross-Section Database
495 for Gas Retrieval in the UV-Visible-Near IR Range, Applied to the GOMOS Retrieval Algorithm AerGOM, Frontiers in Environmental Science, 7, 1–18, https://doi.org/10.3389/fenvs.2019.00118, 2019.

Boucher, O.: Atmospheric Aerosols, Springer Netherlands, Dordrecht, https://doi.org/10.1007/978-94-017-9649-1, 2015.

Bourassa, A. E., Rieger, L. A., Lloyd, N. D., and Degenstein, D. A.: Odin-OSIRIS stratospheric aerosol data product and SAGE III intercomparison, Atmospheric Chemistry and Physics, 12, 605–614, https://doi.org/10.5194/acp-12-605-2012, 2012.

500 Brühl, C., Lelieveld, J., Crutzen, P. J., and Tost, H.: The role of carbonyl sulphide as a source of stratospheric sulphate aerosol and its impact on climate, Atmospheric Chemistry and Physics, 12, 1239–1253, https://doi.org/10.5194/acp-12-1239-2012, 2012.

Brühl, C., Lelieveld, J., Tost, H., Höpfner, M., and Glatthor, N.: Stratospheric sulfur and its implications for radiative forcing simulated by the chemistry climate model EMAC, Journal of Geophysical Research, 120, 2103–2118, https://doi.org/10.1002/2014JD022430, 2015.

Brühl, C., Schallock, J., Klingmüller, K., Robert, C., Bingen, C., Clarisse, L., Heckel, A., and North, P.: Stratospheric aerosol radiative
505 forcing simulated by the chemistry climate model EMAC using aerosol CCI satellite data, Atmospheric Chemistry and Physics, 18, 1–15, https://doi.org/https://doi.org/10.5194/acp-18-12845-2018, 2018.

Carn, S. A., Clarisse, L., and Prata, A. J.: Multi-decadal satellite measurements of global volcanic degassing, Journal of Volcanology and Geothermal Research, 311, 99–134, https://doi.org/10.1016/j.jvolgeores.2016.01.002, 2016.

Crutzen, P. J.: The possible importance of CSO for the sulfate layer of the stratosphere, Geophysical Research Letters, 3, 73–76,
510 https://doi.org/10.1029/GL003i002p00073, 1976.

Diehl, T., Heil, A., Chin, M., Pan, X., Streets, D., Schultz, M., and Kinne, S.: Anthropogenic, biomass burning, and volcanic emissions of black carbon, organic carbon, and SO2 from 1980 to 2010 for hindcast model experiments, Atmospheric Chemistry and Physics Discussions, 12, 24 895–24 954, https://doi.org/10.5194/acpd-12-24895-2012, 2012.

Dietmüller, S., Jöckel, P., Tost, H., Kunze, M., Gellhorn, C., Brinkop, S., Frömming, C., Ponater, M., Steil, B., Lauer, A., and Hendricks, J.: A
new radiation infrastructure for the Modular Earth Submodel System (MESSy, based on version 2.51), Geoscientific Model Development,
9, 2209–2222, https://doi.org/10.5194/gmd-9-2209-2016, 2016.

Fischer, H., Birk, M., Blom, C., Carli, B., Carlotti, M., von Clarmann, T., Delbouille, L., Dudhia, A., Ehhalt, D., Endemann, M., Flaud,
J. M., Gessner, R., Kleinert, A., Koopman, R., Langen, J., López-Puertas, M., Mosner, P., Nett, H., Oelhaf, H., Perron, G., Remedios, J.,
Ridolfi, M., Stiller, G., and Zander, R.: MIPAS: an instrument for atmospheric and climate research, Atmospheric Chemistry and Physics,
8, 2151–2188, https://doi.org/10.5194/acp-8-2151-2008, 2008.

Fromm, M., Peterson, D., and Di Girolamo, L.: The Primary Convective Pathway for Observed Wildfire Emissions in the Upper Tro-
posphere and Lower Stratosphere: A Targeted Reinterpretation, Journal of Geophysical Research: Atmospheres, 124, 13 254–13 272,
https://doi.org/10.1029/2019JD031006, 2019.

Giorgetta, M. A., Manzini, E., and Roeckner, E.: Forcing of the quasi-biennial oscillation from a broad spectrum of atmospheric waves,
Geophysical Research Letters, 29, 86–1–86–4, https://doi.org/10.1029/2002GL014756, 2002.

Giorgetta, M. A., Manzini, E., Roeckner, E., Esch, M., and Bengtsson, L.: Climatology and forcing of the quasi-biennial oscillation in the
MAECHAM5 model, Journal of Climate, 19, 3882–3901, https://doi.org/10.1175/JCLI3830.1, 2006.

Glantz, P., Bourassa, A., Herber, A., Iversen, T., Karlsson, J., and Kirkevåg, A.: Remote sensing of aerosols in the Arc-
tic for an evaluation of global climate model simulations, Journal of Geophysical Research: Atmospheres, 119, 8169–8188,
https://doi.org/10.1002/2013JD021279.Received, 2014.

Glatthor, N., Höpfner, M., Baker, I. T., Berry, J., Campbell, J. E., Kawa, S. R., Krysztofiak, G., Leyser, A., Sinnhuber, B.-M., Stiller, G. P.,
Stinecipher, J., and Von Clarmann, T.: Tropical sources and sinks of carbonyl sulfide observed from space, Geophysical Research Letters,
42, 10,082–10,090, https://doi.org/10.1002/2015GL066293, 2015.

Glatthor, N., Höpfner, M., Leyser, A., Stiller, G. P., Von Clarmann, T., Grabowski, U., Kellmann, S., Linden, A., Sinnhuber, B. M.,
Krysztofiak, G., and Walker, K. A.: Global carbonyl sulfide (OCS) measured by MIPAS/Envisat during 2002-2012, Atmospheric Chem-
istry and Physics, 17, 2631–2652, https://doi.org/10.5194/acp-17-2631-2017, 2017.

Grainger, R. G., Lambert, A., Rodgers, C. D., Taylor, F. W., and Deshler, T.: Stratospheric aerosol effective radius, surface area and volume
estimated from infrared measurements, Journal of Geophysical Research, 100, 16 507–16 518, https://doi.org/10.1029/95JD00988, 1995.

Höpfner, M., Glatthor, N., Grabowski, U., Kellmann, S., Kiefer, M., Linden, A., Orphal, J., Stiller, G. P., von Clarmann, T., Funke, B., and
Boone, C. D.: Sulfur dioxide (SO2) as observed by MIPAS/Envisat: temporal development and spatial distribution at 15–45km altitude,
Atmospheric Chemistry and Physics, 13, 10 405–10 423, https://doi.org/10.5194/acp-13-10405-2013, 2013.

Höpfner, M., Boone, C. D., Funke, B., Glatthor, N., Grabowski, U., Günther, A., Kellmann, S., Kiefer, M., Linden, A., Lossow, S., Pumphrey,
H. C., Read, W. G., Roiger, A., Stiller, G. P., Schlager, H., Von Clarmann, T., and Wissmüller, K.: Sulfur dioxide (SO2) from MIPAS in the
upper troposphere and lower stratosphere 2002–2012, Atmospheric Chemistry and Physics, 15, 7017–7037, https://doi.org/10.5194/acp-
15-7017-2015, 2015.

IPCC: 2013: Climate Change 2013: The Physical Science Basis. Contribution of Working Group I to the Fifth Assessment Report of
the Intergovernmental Panel on Climate Change, Cambridge University Press, Cambridge, United Kingdom and New York, NY, USA,
https://doi.org/10.1017/CBO9781107415324, 2013.

Jöckel, P., Sander, R., Kerkweg, A., Tost, H., and Lelieveld, J.: Technical Note: The Modular Earth Submodel System (MESSy) – a new
approach towards Earth System Modeling, Atmospheric Chemistry and Physics, 4, 7139–7166, https://doi.org/10.5194/acpd-4-7139-2004,
2005.

Jöckel, P., Tost, H., Pozzer, A., Brühl, C., Buchholz, J., Ganzeveld, L., Hoor, P., Kerkweg, A., Lawrence, M. G., Sander, R., Steil, B., Stiller, G., Tanarhte, M., Taraborrelli, D., van Aardenne, J., and Lelieveld, J.: The atmospheric chemistry general circulation model ECHAM5/MESSy1: consistent simulation of ozone from the surface to the mesosphere, Atmospheric Chemistry and Physics, 6, 6957–7050, https://doi.org/10.5194/acpd-6-6957-2006, 2006.

Jöckel, P., Kerkweg, A., Pozzer, A., Sander, R., Tost, H., Riede, H., Baumgaertner, A., Gromov, S., and Kern, B.: Development cycle 2 of the Modular Earth Submodel System (MESSy2), Geoscientific Model Development, 3, 717–752, https://doi.org/10.5194/gmd-3-717-2010, 2010.

Junge, C. E., Chagnon, C. W., and Manson, J. E.: Stratospheric aerosols, Journal of Meteorology, 18, 81–108, https://doi.org/10.1175/1520-0469(1961)018, 1961.

Kerkweg, A.: Global Modelling of Atmospheric Halogen Chemistry in the Marine Boundary Layer, Ph.D. thesis, Friedrich-Wilhelms-Universität Bonn, 2005.

Kerkweg, A., Buchholz, J., Ganzeveld, L., Pozzer, A., Tost, H., and Jöckel, P.: Technical Note: An implementation of the dry removal processes DRY DEPosition and SEDImentation in the Modular Earth Submodel System (MESSy), Atmospheric Chemistry and Physics, 6, 6853–6901, https://doi.org/10.5194/acpd-6-6853-2006, 2006a.

Kerkweg, A., Sander, R., Tost, H., and Jöckel, P.: Technical Note: Implementation of prescribed (OFFLEM), calculated (ONLEM), and pseudo-emissions (TNUDGE) of chemical species in the Modular Earth Submodel System (MESSy), Atmospheric Chemistry and Physics, 6, 5485–5504, https://doi.org/10.5194/acpd-6-5485-2006, 2006b.

Kettle, A. J. and Andreae, M. O.: Flux of dimethylsulfide from the oceans: A comparison of updated data sets and flux models, Journal of Geophysical Research, 105, 26 793–26 808, https://doi.org/10.1029/2000JD900252, 2000.

Klingmüller, K., Metzger, S., Abdelkader, M., Karydis, V. A., Stenchikov, G. L., Pozzer, A., and Lelieveld, J.: Revised mineral dust emissions in the atmospheric chemistry–climate model EMAC (MESSy 2.52 DU_Astitha1 KKDU2017 patch), Geoscientific Model Development, 11, 989–1008, https://doi.org/10.5194/gmd-11-989-2018, 2018.

Kyrölä, E., Tamminen, J., Sofieva, V., Bertaux, J. L., Hauchecorne, A., Dalaudier, F., Fussen, D., Vanhellemont, F., Fanton D'Andon, O., Barrot, G., Guirlet, M., Fehr, T., and Saavedra De Miguel, L.: GOMOS O3, NO2, and NO3 observations in 2002-2008, Atmospheric Chemistry and Physics, 10, 7723–7738, https://doi.org/10.5194/acp-10-7723-2010, 2010.

Metzger, S. and Lelieveld, J.: Reformulating atmospheric aerosol thermodynamics and hygroscopic growth into haze and clouds, Atmospheric Chemistry and Physics, 7, 849–910, https://doi.org/10.5194/acpd-7-849-2007, 2007.

Mills, M. J., Schmidt, A., Easter, R., Solomon, S., Kinnison, D. E., Ghan, S. J., Neely, R. R., Marsh, D. R., Conley, A., Bardeen, C. G., and Gettelman, A.: Global volcanic aerosol properties derived from emissions, 1990-2014, using CESM1(WACCM), Journal of Geophysical Research, 121, 2332–2348, https://doi.org/10.1002/2015JD024290, 2016.

Minnis, P., Harrison, E. F., Stowe, L. L., Gibson, G. G., Denn, F. M., Doelling, D. R., and Smith, W. L.: Radiative climate forcing by the Mount Pinatubo eruption, Science, 259, 1411–1415, https://doi.org/10.1126/science.259.5100.1411, 1993.

Neely, R. R., English, J. M., Toon, O. B., Solomon, S., Mills, M., and Thayer, J. P.: Implications of extinction due to meteoritic smoke in the upper stratosphere, Geophysical Research Letters, 38, 1–6, https://doi.org/10.1029/2011GL049865, 2011.

Nordeng, T. E.: Extended version of the convective parametrization scheme at ECMWF and their impact on the mean and transient activity of the model in the tropics, Tech. rep., ECMWF, Reading, 1994.

Pozzer, A., Jöckel, P., Sander, R., Williams, J., Ganzeveld, L., and Lelieveld, J.: Technical Note: The MESSy-submodel AIRSEA calculating the air-sea exchange of chemical species, Atmospheric Chemistry and Physics, 6, 5435–5444, https://doi.org/10.5194/acp-6-5435-2006, 2006.

Pringle, K. J., Tost, H., Metzger, S., Steil, B., Giannadaki, D., Nenes, A., Fountoukis, C., Stier, P., Vignati, E., and Lelieveld, J.: Description and evaluation of GMXe: a new aerosol submodel for global simulations (v1), Geoscientific Model Development, 3, 391–412, https://doi.org/10.5194/gmd-3-391-2010, 2010.

Rieger, L. A., Bourassa, A. E., and Degenstein, D. A.: Merging the OSIRIS and SAGE II stratospheric aerosol records, Journal of Geophysical Research, 120, 8890–8904, https://doi.org/10.1002/2015JD023133, 2015.

Rieger, L. A., Malinina, E. P., Rozanov, A. V., Burrows, J. P., Bourassa, A. E., and Degenstein, D. A.: A study of the approaches used to retrieve aerosol extinction, as applied to limb observations made by OSIRIS and SCIAMACHY, Atmospheric Measurement Techniques, 11, 3433–3445, https://doi.org/10.5194/amt-11-3433-2018, 2018.

Rieger, L. A., Zawada, D. J., Bourassa, A. E., and Degenstein, D. A.: A Multiwavelength Retrieval Approach for Improved OSIRIS Aerosol Extinction Retrievals, Journal of Geophysical Research: Atmospheres, 124, 2018JD029 897, https://doi.org/10.1029/2018JD029897, 2019.

Robert, C. É., Bingen, C., Vanhellemont, F., Mateshvili, N., Dekemper, E., Tétard, C., Fussen, D., Bourassa, A., and Zehner, C.: AerGOM, an improved algorithm for stratospheric aerosol retrieval from GOMOS observations. Part 2: Intercomparisons, Atmospheric Measurement Techniques, 9, 4701–4718, https://doi.org/10.5194/amt-2016-27, 2016.

Roeckner, E., Bäuml, G., Bonaventura, L., Brokopf, R., Esch, M., Giorgetta, M., Hagemann, S., Kirchner, I., Kornblueh, L., Rhodin, A., Schlese, U., Schulzweida, U., Tompkins, A., Manzini, E., Rhodin, A., Schlese, U., Schulzweida, U., and Tompkins, A.: The atmospheric general circulation model ECHAM5. Part I: Model description., Tech. Rep. 349, Max-Planck-Institute für Meteorologie, Hamburg, https://doi.org/10.1029/2010JD014036, 2003.

Roeckner, E., Brokopf, R., Esch, M., Giorgetta, M. A., Hagemann, S., Kornblueh, L., Manzini, E., Schlese, U., and Schulzweida, U.: Sensitivity of simulated climate to horizontal and vertical resolution in the ECHAM5 atmosphere model, Journal of Climate, 19, 3771–3791, https://doi.org/10.1175/JCLI3824.1, 2006.

Sander, R., Baumgaertner, A., Gromov, S., Harder, H., Jöckel, P., Kerkweg, A., Kubistin, D., Regelin, E., Riede, H., Sandu, A., Taraborrelli, D., Tost, H., and Xie, Z.-Q. Q.: The atmospheric chemistry box model CAABA/MECCA-3.0, Geoscientific Model Development, 4, 373–380, https://doi.org/10.5194/gmd-4-373-2011, 2011.

Santer, B. D., Bonfils, C., Painter, J. F., Zelinka, M. D., Mears, C., Solomon, S., Schmidt, G. A., Fyfe, J. C., Cole, J. N., Nazarenko, L., Taylor, K. E., and Wentz, F. J.: Volcanic contribution to decadal changes in tropospheric temperature, Nature Geoscience, 7, 185–189, https://doi.org/10.1038/ngeo2098, 2014.

Schneider, J., Weigel, R., Klimach, T., Dragoneas, A., Appel, O., Hünig, A., Molleker, S., Köllner, F., Clemen, H.-C., Eppers, O., Hoppe, P., Hoor, P., Mahnke, C., Krämer, M., Rolf, C., Grooß, J.-U., Zahn, A., Obersteiner, F., Ravegnani, F., Ulanovsky, A., Schlager, H., Scheibe, M., Diskin, G. S., DiGangi, J. P., Nowak, J. B., Zöger, M., and Borrmann, S.: Aircraft-based observation of meteoric material in lower-stratospheric aerosol particles between 15 and 68° N, Atmospheric Chemistry and Physics, 21, 989–1013, https://doi.org/10.5194/acp-21-989-2021, 2021.

Solomon, S., Daniel, J. S., Neely, R. R., Vernier, J.-P., Dutton, E. G., and Thomason, L. W.: The persistently variable "background" stratospheric aerosol layer and global climate change, Science, 333, 866–870, https://doi.org/10.1126/science.1206027, 2011.

625 Stier, P., Feichter, J., Kinne, S., Kloster, S., Vignati, E., Wilson, J., Ganzeveld, L., Tegen, I., and Werner, M.: The aerosol-climate model ECHAM5-HAM, Atmospheric Chemistry and Physics, 5, 1125–1156, 2005.

Thomason, L. W., Burton, S. P., Luo, B. P., and Peter, T.: SAGE II measurements of stratospheric aerosol properties at non-volcanic levels, Atmospheric Chemistry and Physics, 8, 983–995, 2008.

Tiedtke, M.: A Comprehensive Mass Flux Scheme for Cumulus Parameterization in Large-Scale Models, Monthly Weather Review, 117, 1779–1800, https://doi.org/10.1175/1520-0493(1989)117<1779:ACMFSF>2.0.CO;2, 1989.

Timmreck, C.: Modeling the climatic effects of large explosive volcanic eruptions, Wiley Interdisciplinary Reviews: Climate Change, 3, 545–564, https://doi.org/10.1002/wcc.192, 2012.

Timmreck, C., Graf, H. F., and Feichter, J.: Simulation of Mt. Pinatubo volcanic aerosol with the Hamburg climate model ECHAM4, Theoretical and Applied Climatology, 62, 85–108, https://doi.org/10.1007/s007040050076, 1999.

635 Tost, H., Jöckel, P., Kerkweg, A., Sander, R., and Lelieveld, J.: Technical note: A new comprehensive SCAVenging submodel for global atmospheric chemistry modelling, Atmospheric Chemistry and Physics, 5, 11 157–11 181, https://doi.org/10.5194/acpd-5-11157-2005, 2006a.

Tost, H., Jöckel, P., and Lelieveld, J.: Influence of different convection parameterisations in a GCM, Atmospheric Chemistry and Physics, 6, 5475–5493, https://doi.org/10.5194/acp-6-5475-2006, 2006b.

640 Tost, H., Jöckel, P., and Lelieveld, J.: Lightning and convection parameterisations - uncertainties in global modelling, Atmospheric Chemistry and Physics, 7, 4553–4568, https://doi.org/10.5194/acpd-7-6767-2007, 2007.

Tost, H., Lawrence, M. G., Brühl, C., and Jöckel, P.: Uncertainties in atmospheric chemistry modelling due to convection parameterisations and subsequent scavenging, Atmospheric Chemistry and Physics, 10, 1931–1951, https://doi.org/10.5194/acp-10-1931-2010, 2010.

Vanhellemont, F., Fussen, D., and Bingen, C.: Global one-step inversion of satellite occultation measurements: A practical method, Journal 645 of Geophysical Research, 109, D09 306, https://doi.org/10.1029/2003JD004168, 2004.

Vanhellemont, F., Fussen, D., Mateshvili, N., Tétard, C., Bingen, C., Dekemper, E., Loodts, N., Kyrölä, E., Sofieva, V., Tamminen, J., Hauchecorne, A., Bertaux, J. L., Dalaudier, F., Blanot, L., Fanton D'Andon, O., Barrot, G., Guirlet, M., Fehr, T., and Saavedra, L.: Optical extinction by upper tropospheric/stratospheric aerosols and clouds: GOMOS observations for the period 2002-2008, Atmospheric Chemistry and Physics, 10, 7997–8009, https://doi.org/10.5194/acp-10-7997-2010, 2010.

650 Vanhellemont, F., Mateshvili, N., Blanot, L., Robert, C. É., Bingen, C., Sofieva, V., Dalaudier, F., Tétard, C., Fussen, D., Dekemper, E., Kyrölä, E., Laine, M., Tamminen, J., and Zehner, C.: AerGOM, an improved algorithm for stratospheric aerosol retrieval from GOMOS observations. Part 1: Algorithm description, Atmospheric Measurement Techniques, 2016, 1–24, https://doi.org/10.5194/amt-2016-27, 2016.

Vehkamäki, H., Kulmala, M., Napari, I., Lehtinen, K. E. J., Timmreck, C., Noppel, M., and Laaksonen, A.: An improved parameterization 655 for sulfuric acid – water nucleation rates for tropospheric and stratospheric conditions, Journal of Geophysical Research, 107, 1–10, https://doi.org/10.1029/2002JD002184, 2002.

Vernier, J.-P., Fairlie, T. D., Deshler, T., Natarajan, M., Knepp, T., Foster, K., Wienhold, F. G., Bedka, K. M., Thomason, L., and Trepte, C.: In situ and space-based observations of the Kelud volcanic plume: The persistence of ash in the lower stratosphere, Journal of Geophysical Research : Atmospheres, 121, 104–118, https://doi.org/10.1002/2016JD025344, 2016.

660 Vignati, E., Wilson, J., and Stier, P.: M7: An efficient size-resolved aerosol microphysics module for large-scale aerosol transport models, Journal of Geophysical Research: Atmospheres, 109, https://doi.org/10.1029/2003JD004485, 2004.

Wong, T., Wielicki, B. A., Lee, R. B., Smith, G. L., Bush, K. A., and Willis, J. K.: Reexamination of the observed decadal variability of the earth radiation budget using altitude-corrected ERBE/ERBS nonscanner WFOV data, Journal of Climate, 19, 4028–4048, https://doi.org/10.1175/JCLI3838.1, 2006.